Engineering Failure Analysis 150 (2023) 107295

Contents lists available at ScienceDirect

Engineering Failure Analysis

journal homepage: www.elsevier.com/locate/engfailanal

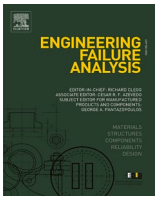

Diagonal compression testing of masonry under fatigue loading and high static loads

Georgios Karanikoloudis [a,*], João B. Serra [b], Paulo B. Lourenço [a]

[a] Department of Civil Engineering, University of Minho, Guimarães, Portugal
[b] National Laboratory of Civil Engineering, Department of Geotechnics, Lisbon, Portugal

ARTICLE INFO

Keywords:
Civil engineering
Historic brick masonry with lime mortar
Fatigue
Experimental diagonal compression fatigue tests
Induced ground-borne vibrations
Stiffness degradation
Strain relaxation

ABSTRACT

Underground railway operations pose a significant impact on overlying, highly sensitive historic masonry structures. Here, the process of structural assessment involves fatigue actions, through induced ground-borne vibrations, from operating underground railways. Considering long-term exposure periods, fatigue can introduce local cracking and losses, which endanger the integrity of both structural and non-structural elements. The lack of experimental fatigue data on tensile actions in masonry and the apparent computational restraints from constitutive cementitious material models that do not account for damage due to repeated loading, increase the complexity of structural assessment, under combined fatigue actions and other hazards. The current paper aims at providing new experimental data on fatigue in historic brick and lime mortar masonry wallets, replicating realistic combinations of static and fatigue loading under diagonal compression. Material deterioration and stiffness degradation are monitored throughout the process. Hence, under moderate amplitudes of fatigue loading and high static loads, cracking occurred, at a relatively low number of cycles, demonstrating the need for more strict vibration thresholds to ensure the integrity of historic masonry buildings.

Introduction

Scope of study

The current work is focused on experimental fatigue quasi-static cyclic tests on brick masonry wallets with single face rendering, composed of solid bricks and lime mortar, and considered as replicas for historic brick masonry. Given the damaging effects of tension and shear for masonry, fatigue loading protocols were designed under diagonal compression fatigue testing, with the following main objectives and expected results:

- Document and assess the current knowledge on the fatigue studies in brick masonry.
- Generate acquisition data on the response of a specific brick masonry typology, under quasistatic fatigue diagonal compression loading, in combination with high static shear stress and low to medium stress reversals.
- Monitor changes on the material properties of brick masonry, regarding load capacity and softening.

* Corresponding author at: ISISE, Department of Civil Engineering, University of Minho, Campus de Azurém, Guimarães 4800-058, Portugal.
E-mail addresses: id5702@alunos.uminho.pt (G. Karanikoloudis), biles@lnec.pt (J.B. Serra), pbl@civil.uminho.pt (P.B. Lourenço).

https://doi.org/10.1016/j.engfailanal.2023.107295
Received 11 February 2023; Received in revised form 20 April 2023; Accepted 26 April 2023
Available online 4 May 2023

Nomenclature

Symbols:

A, B, C, D, b, g, h, p, q	Numeric constants
a	Peak particle acceleration in oscillatory motion
A_σ	Amplitude ratio of stress amplitude σ_a to mean static stress σ_m
c	Wave velocity
d	Peak particle displacement in oscillatory motion
d_o	Peak displacement amplitude during an elastic sinusoidal waveform
f	Excitation frequency of oscillation
f	Loading frequency
F	Vertical force applied along the diagonal of a wallet, during a diagonal compression test
f_c	Nominal compressive strength of masonry
f_t	Nominal tensile strength of masonry, here retrieved from diagonal compression in wallets
G_c	Fracture energy in compression
G_f	Fracture energy in tension
G_{mod}	Shear modulus
G_{sec}	Secant shear stiffness
k	Angular wavenumber of the wave
LVDT	Linear variable differential transformer
N_f	Number of cycles for fatigue failure, under a combination of σ_m and σ_a
R	Stress ratio of minimum σ_{min} to maximum stress σ_{max} amplitude
S	Amplitude ratio of maximum stress amplitude σ_{max} to mean static stress σ_m
SG	Strain gauge
T	Temperature
T_f	Cyclic loading period
v	Peak particle velocity in oscillatory motion
v_o	Peak velocity amplitude during an elastic sinusoidal waveform
$\gamma_{t,m}$	Average shear strain, from fatigue shear strain envelopes
γ_t	Shear strain
Δ_ε	Strain range of a sinusoidal cyclic load
Δ_σ	Stress range of a sinusoidal cyclic load
ε	Strain
ε_a	Strain amplitude of a sinusoidal cyclic load
η	Poisson ratio
λ	Slope
σ_a	Stress amplitude of a sinusoidal cyclic load
σ_m	Mean static stress
σ_{max}	Maximum stress amplitude of a sinusoidal cyclic load
σ_{min}	Minimum stress amplitude of a sinusoidal cyclic load
ω	Radial frequency of oscillation

- Formulate analytical relations for fatigue deterioration in masonry structures, based on the evolution of shear strain and shear modulus and assess the residual life for fatigue combinations that do not result to failure.

Research background

Dynamically induced moderate stress–strain variations, due to operational fatigue conditions, are characteristic for many historic masonry structures, yet not fully investigated. These variations have long-term effects on ductility, durability, stiffness and strain increase. Indeed, structural deterioration due to fatigue is a result of inelastic strain accumulation between mortar and brick, being likely that the tensile strength of brick units also deteriorates [1].

Ground-borne induced vibrations, which reach the foundation level of the buildings of interest, are caused by quasi-static and dynamic axial loads from underground moving trains. Vibration limits in international standards, target immediate or fatigue damage for serviceability limit states, with strict, yet variable, thresholds for cultural heritage buildings [39,10,25,54,34]. In these buildings, monitoring of structural conditions or actions is essential to the knowledge of structural response, as demonstrated in Karanikoloudis et al. [41].

Fatigue, based on [32], can be defined as the process of initiation and propagation of damage in structural parts, due to frequently repeated actions, resulting in failure at a lower level than the ultimate quasi-static loads. In the laboratory, a force-controlled fatigue test is usually designed under a continuous cyclic load, namely of a sinusoidal function. Considering the transient, intermittent and

pseudo-steady state nature of ground-borne vibrations, the duration of a fatigue experimental test should cover a sufficient number of vibration amplitudes, e.g., 10^5-10^{10} cycles [25,49,18]. Basic parameters are the loading frequency f and period T_f, whereas the fatigue strength $\Delta\sigma$ or else $2\sigma_a$ is the stress range of the cyclic load, linked to a static stress state σ_m and a number of cycles N_f, presented in Fig. 1a, with corresponding stress ratios R, A_σ and S in Equation (1) [11]. Given the high variability of fatigue strength, a high number of specimens is needed, e.g., five samples, regarding fatigue testing in reinforcement bars, girders, welded wire mesh etc. [11]. As demonstrated in Koltsida et al. [42], a three-stage strain rate is identified in masonry, i.e., a rapid increase until 10% of the normalized fatigue life N/N_f (Stage I), a steady increase until 80–90% of N/N_f (Stage II), and a final rapid increase (Stage III) (Fig. 1b).

Fatigue in the Ultimate Limit State (ULS) is based on semi-logarithmic S-N_f (also $\Delta\sigma$ or σ_a – $logN_f$) curves, either compressive or tensile. Their definition is performed by means of a reliability-based assessment, accounting for the distribution of experimental data, e.g., a survival probability of 95%. Fatigue life S-N_f curves can be approximated either with the generic relations of Equations 2–3 and Equations 4–5, with a linear curve under a log-linear and log–log plot respectively, where A, B, C and D are numeric constants [26,18,19]. If, for a significant number of cycles ($\simeq 10^7$), no failure occurs, a constant branch is added, defined as endurance limit [17]. According to BD 91/04-14 [6] and serviceability assessment criteria for compressive stresses in unreinforced masonry bridges, this limit for S is set at $0.5f_c$, while from experimental fatigue tests in scaled masonry arches, in [46], is set around $0.4f_c$. Similar limits may be established for shear or tensile fatigue stresses. The completion of fatigue laboratory testing for a range of mean static stresses σ_{mi} and stress range amplitudes σ_{ai}, can provide fatigue life plots, as represented in Fig. 1c.

$$R = \sigma_{min}/\sigma_{max},\ A_\sigma = \sigma_a/\sigma_m,\ S = \sigma_{max}/f_c \tag{1}$$

$$\sigma_a = A - B \bullet log(N_f) \tag{2}$$

$$log(S) = A - B \bullet logN_f{}^{(1-R)} \tag{3}$$

$$\sigma_a = C \bullet N_f{}^{D} \tag{4}$$

$$S = C \bullet N_f{}^{-D(1-R)} \tag{5}$$

Experimental fatigue tests on masonry specimens can be found in [18,19,42,43,16,46,52,53]. In Roberts et al. [52], a deterministic

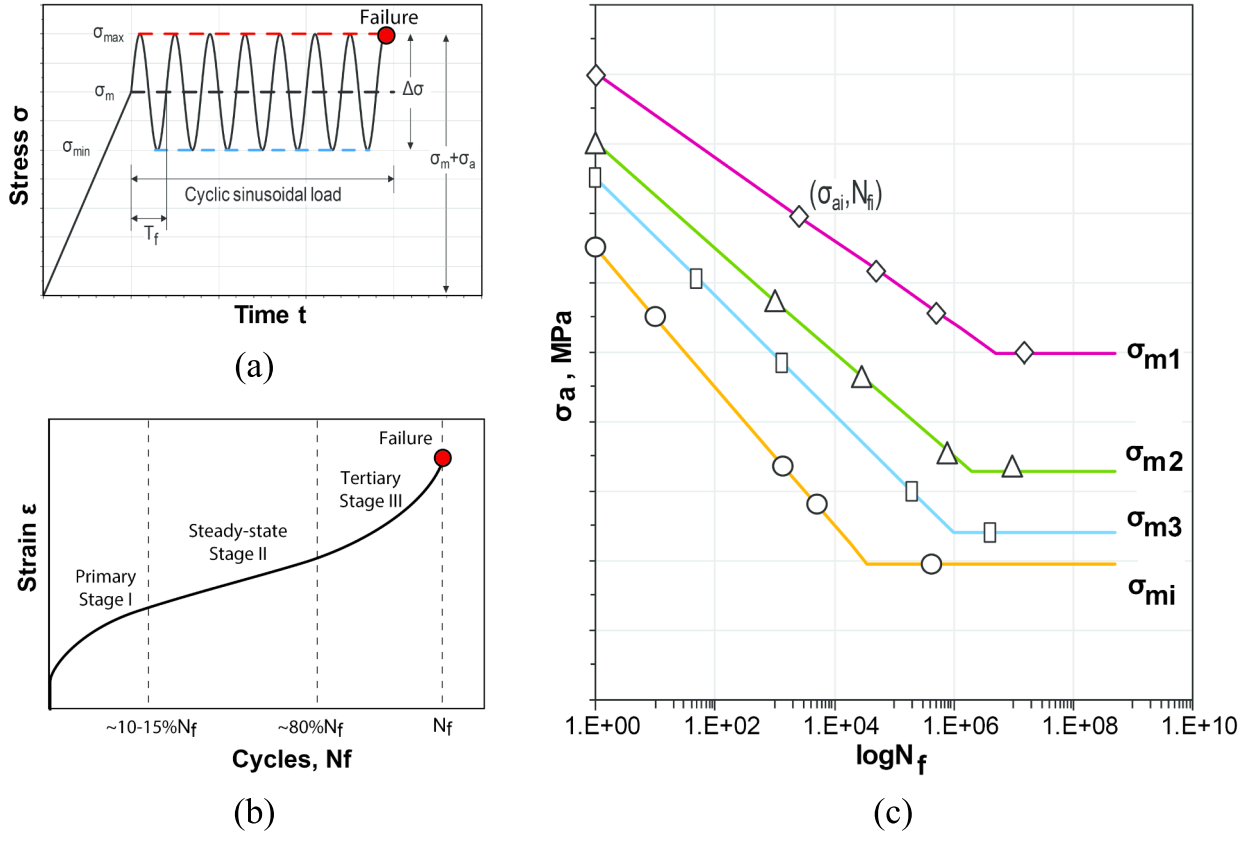

Fig. 1. Laboratory accelerated fatigue tests: (a) equivalent fatigue loading under a constant amplitude, sinusoidal pattern; (b) three stages of fatigue strain, under constant fatigue stress; (c) semi-log plots of fatigue life, under different static stress levels σ_{mi}, vs. number of cycles N_f.

fatigue strength function, was derived from the linear lower bound of high stress rate fatigue tests on masonry prisms in compression, under submerged, wet and dry conditions, with the cyclic frequency of 5 Hz. In Koltsida et al. [42], fatigue tests of uniaxial compression were performed in brick masonry prisms with cement and lime mortar, under a cyclic frequency of 2 Hz, with σ_{min} equal to $0.1f_c$ and σ_{max} varying within 0.55–0.80f_c. In Carpinteri et al. [16], fatigue tests were performed under direct cyclic shear tests in masonry specimens, with a load ratio S equal to 0.30, 0.50 and 0.70 of f_c and a cyclic frequency of 1–2 Hz. In Melbourne et al. [46], cyclic fatigue tests were performed on multi-ring brick masonry segmental arches with cement-lime mortar. The cyclic fatigue loading, applied as point loads at ¼ and ¾ of the arch's span, was executed in a range of $2x10^4$ to $2x10^6$ cycles, with maximum fatigue stresses within the range of 0.28–0.60f_c, and a cyclic frequency of 2 Hz. Here, instead of the prevalent four-hinge static failure, the fatigue failure was the ring separation or slippage. In Ronca et al. [53], experimental tests on fatigue loading in masonry prisms, perpendicular to the bed joints were conducted under medium to high static compression (0.55–0.80f_c), with fatigue stress ratios varying from 0.05 to $0.1f_c$ and cyclic frequencies of 1, 5 and 10 Hz. Here, axial deformations increased with the increase of cyclic frequencies and the strain rate in all tested frequencies exhibits a linear trend for static loads up to $0.65f_c$. For samples tested under fatigue a stress ratio of $0.05f_c$ and a static stress of $0.8f_c$ sudden explosive failure occurred after a relatively small number of cycles.

Research basis, motivation and methodology

The current accelerated fatigue experimental tests, assumed the scenario of ground-borne vibrations, and were designed under diagonal compression loading regimes, in brick and lime mortar masonry wallets, also considering the presence of a lime-based render in one side. The main objective was set on pairing the loading stress levels (σ_m), the stress range levels ($\pm\sigma_a$) and the number of cycles (N_f) to certain quantifiable levels of damage, amplitudes of ground-borne vibrations, stiffness degradation and failure. Reference envelope curves of diagonal compression, for each of the specimens tested under fatigue, were constructed partly from preliminary quasi-static, cyclic loading, and partly from curve fitting, under statistically normalized stress–strain relationships, from both rendered and non-rendered wallets. Loading protocols were set under a high static shear stress and low to medium stress reversals, considering realistic scenarios of shear stress concentrations at specific locations of a masonry façade, with the masonry at a nonlinear state and a moderate capacity margin. Also, for each tested wallet, instead of an independent loading regime for fatigue, an alternative scenario was investigated, under time-based variations of static stress and strain, which, according to Binda [7], are common in the course of time for many historic structures, e.g., a dead load increase from structural interventions and a change of load paths from settlements, earthquakes or accidental actions.

Reference ground-borne vibration thresholds from [25] were used, in order to move from the targeted peak particle velocity (ppv) values, under a characteristic wave frequency range, to the targeted displacement and corresponding force amplitudes of fatigue loading, by means of stiffness functions. In total, each specimen was subjected to several fatigue loading combinations, of varying static and constant cyclic stresses in diagonal compression, until failure was reached.

For each masonry wallet, tested under fatigue in diagonal compression, and until failure after N_f cycles, shear strain–time histories were found temperature dependent, following complex contractions and dilations, and thus, were linearly compensated by means of simultaneous readings from temperature sensors.

Following, fatigue data were processed individually for each loading combination, based on shear strain γ_t relaxation and secant shear stiffness G_{sec} softening, and fatigue curves of γ_t-N_f, G_{sec}-N_f and normalized correlations were constructed, according to Dowling [26], Glinka [35], and Hu et al. [38]. Hence, the possibility of fatigue inflicted damage can be verified, under positive and negative rates in shear strains and secant shear stiffness respectively. Eventually, fatigue shear strains and secant shear stiffness evolve exponentially, and the masonry fractures and collapses [38,35].

Finally, the average shear strain γ_t and secant shear stiffness G_{sec} results, were fitted with a reversed non-symmetrical sigmoid function. Considering the hypothesis of Holmen [36], of equal fatigue failure properties, end-to-end linear piecewise functions of normalized fatigue properties estimated the fatigue life of fatigue stress states, in the cases that failure was not reached.

Materials and methods

Material constituents

The current experimental work focuses on replicas of historic masonry wallets of the 19th-20th centuries, with solid, low fired bricks and lime mortar. Historic solid fired clay bricks can exhibit a compressive strength f_c between 5 and 25 MPa, and firing temperatures were usually in the order of 1000 °C, while the tensile strength and the Young's modulus, vary within the range of 3%-13.5% f_c and 125–1400 f_c respectively [22] and Fernandes et al. (2009). Considering historic mortars, the typical component is aerial lime, usually with pozzolanic additives. Additional components are sand, aggregates and water, the latter in proportions of 15–20% in mass [22]. Their uniaxial compression strength is within the ranges of 0.5–2.5 MPa, which under modern code specifications, can be designated as M2 and M4 class of NA to BS EN 1996-1-1: 2005 [47] or as CS I and CS II mortar in EN 998-1:2016 [29].

Under the current framework, solid bricks, from the Cenol manufacturing company in Amarante, Portugal were chosen. The bricks were mildly extruded, with dimensions of 200x100x50 mm^3 (length × width × height) and low firing temperatures of 850C. Regarding the lime mortar for the joints and render, a ready lime mortar premix from SecilTek, a Portuguese construction material company, was used, with a classification of M4 and CS II, with a ratio of 1:3 for the lime and sand, respectively, and a water content of 15% [15,29,51,48,12]. Material characterization tests were conducted on mass density, brick water absorption and mean porosity, three-point loading tests for flexural capacity, compression strength tests and tests for Young's modulus, presented in Table 1 and Table 2.

Reference brick masonry typology

Brick architectural works, prevailed in the 19th-20th centuries in Europe, with buildings reaching up to six floors [2,44]. Regarding the behavior of brick masonry, the compressive strength f_c presents a high variation, depending on the relative height, the stiffness and the Poisson's ratio of the brick unit and bed mortar joints [22]. According to NTC [50], the compressive strength f_c of fired clay brick masonry with lime or cementitious mortar is in the range of 2.6–8.0 MPa, while according to Tomazevic [55] the tensile strength f_t is generally low, around 0.03–0.09 of f_c. The in-plane tensile failure of masonry is often determined by a diagonal compression test on a square masonry wallet. Cracks are either formed parallel to the compressive forces, and in the area within the metallic platens, by splitting bricks and mortar joints or progress through sliding within a single bed joint, in cases of poor adhesion between brick and mortar, or a combination of the above [22].

Here, a series of brick masonry wallets were constructed with a Flemish bond, a 1½ brick thickness and a joint thickness of 10–15 mm. To achieve uniformity in workmanship, all wallets were constructed by the same mason, each built within one day. The bricks were soaked in water for 1 h, prior to construction, in order to minimize the absorption of water from the mortar. Once constructed, each wallet was regularly sprayed with water, during 48 h, while for the first 7 days was covered with a polyethylene sheet, so as to maintain RH conditions of around 90% [7,31]. The total curing age, at ambient laboratory conditions, was between 190 and 210 days. The wallets were tested under cyclic uniaxial and diagonal compression, according to BS EN 1052-1-1999 [13] and ASTM E519/E519M-20 [5], with the results presented in Table 3 and Fig. 2.

Test specimen configuration, instrumentation and initial material properties

In total, for the diagonal compression fatigue tests, three brick masonry wallets with lime mortar joints, of size 650 × 650 × 310 mm^3 (width × height × thickness), and plastered only in one side, were built and cured for 200 days, prior to testing. Most of the historic masonry walls carry rendering, primarily lime-based, with a thickness of 10–30 mm, accounting for environmental protection, and as finishes for rubble masonry bonds [24]. For the current experimental work, a lime-based render of 30 mm thickness was chosen. Each wallet is designated as $DCf_{i\text{-}j}$, where i is the wallet's assigned number and j is the sequential part of the fatigue test. For obtaining reference diagonal compression capacity curves, for rendered and non-rendered wallets, of the exact masonry typology and curing conditions, one rendered wallet (DCf_1) was also built and tested until failure, in monotonic diagonal compression.

For the collection of acquisition data, a set of linear variable differential transformers (LVDTs) and Strain Gauges (SGs) were used, attached to the surface of masonry and render (when applicable). A total of six LVDTs were used, for measuring shear strains and global vertical displacements. For the SGs, one or two PL-120-11 single element strain gauges of 120 mm length were attached in masonry, by means of an adhesive resin, and covering three bricks and two corresponding bed joints [23]. The geometric configuration and instrumentation of the $DCf_{i\text{-}j}$ wallets is presented in Fig. 3a.

As seen in Fig. 3b, the wallet DCf_1 fails in diagonal compression, under a diagonal splitting crack, passing through the mortar joints and bricks, while the plaster follows the same splitting pattern, without a detachment at the interface. By accounting only the diagonal elongations from the non-rendered side, the tensile strength f_t and shear modulus G_{mod} are equal to 1.1 MPa and 1.1 GPa respectively, found 3.0 and 1.3 times higher, compared to the respective ones of the non-rendered masonry wallets, of the same material and curing conditions (Table 4). Regarding the lateral strains in masonry, as recorded from the SGs and seen in Fig. 3b, they tend to localize and evolve exponentially in the area of the crack (SG1), while next to the crack (SG2), and right before failure, the tensile strain is reversed, with potential microcracks closing. Such an observation appears consistent with the smeared crack model and the post failure strain localization in the fracture process of brittle materials [27,45].

In order to compare the stress–strain response in diagonal compression of the rendered wallet DCf_1 with the three non-rendered wallets DC_1, DC_2 and DC_3, as seen initially from the graph of Fig. 4a, no correlation is evident, except when values of stress and strain, corresponding to 5%, 33%, 50%, 70%, 80%, 90% and 100% of f_t are normalized, as shown in the graph of Fig. 4b and enumerated in Table 4. Thus, a very similar normalized stress–strain response in diagonal compression is evident, and a statistical

Table 1
Physical and mechanical properties of fired bricks, i.e., mass density, water absorption, mean porosity, compressive strength, flexural strength and Young's modulus.

Low Fired Clay Solid Bricks	Mean Mass Density (kN/m^3)	Mean Water Absorption (%)	Mean Porosity (%)	Compressive strength (MPa)		Flexural strength (MPa)	Young's Modulus (MPa)	
Cubes[1]/Prisms[2] b × d × h[3]	40x40x40/ 40x40x120	40x40x40/ 40x40x120	40x40x40	40x40x (3x40)	40x40x120	200x100x50	40x40x (3x40)	40x40x120
Load path direction Conditions[4]	– Oven dried at 105 °C ± 5 °C for 24 h	–	–	Vertical	Horizontal	Vertical	Vertical	Horizontal
Mean value (#specimen/CoV)	18.1 (27/1.1%)	14.1% (5/5.0%)	26.7% (5/3.6%)	17.17 (6/6.9%)	29.69 (6/2.4%)	3.62 (6/34.1%)	1222 (5/6.5%)	6028 (5/2.8%)

[1]: BS EN 772-1:2011 [14] Methods of test for masonry units. Determination of compressive strength + A1:2015.
[2]: ASTM C67/C67M-20 [4] Standard Test Methods for Sampling and Testing Brick and Structural Clay Tile.
[3]: b: length, d: width, h: height (mm^3).
[4]: BS EN 772-1:2011 [14] Methods of test for masonry units. Determination of compressive strength (+A1:2015 §7.3.3a).

Table 2
Physical and mechanical properties of the adopted NHL mortar, i.e., mass density, compressive strength, flexural strength and Young's modulus.

Cubes/Prisms/Cylinders	Prisms[1]: 40x40x160 (mm^3) Mean Mass Density [kN/m^3] (#specimen/CoV)	Cubes[1]: 40x40x40 (mm^3) Mean Compressive Strength [MPa] (#specimen/CoV)	Prisms[1]: 40x40x160 (mm^3) Mean Flexural Strength [MPa] (#specimen/CoV)	Cylinders[2]: Φ75x150 (mm^3) Mean Young's Modulus [MPa] (#specimen/CoV)
Climatic chamber (60%RH, 20 °C)				
7 days	21.7 (3/0.36%)	1.15 (4/3.28%)	0.44 (3/2.92%)	948 (3/15.38%)
14 days	19.5 (3/0.71%)	2.53 (4/2.8%)	0.96 (3/18.77%)	2613 (3/14.14%)
28 days	19.4 (3/0.53%)	3.17 (4/1.69%)	0.84 (3/8.78%)	3757 (3/10.07%)
56 days	19.4 (3/1.01%)	3.04 (4/6.23%)	0.78 (3/15.49%)	4205 (3/7.06%)
90 days	19.7 (3/0.78%)	3.15 (4/4.71%)	0.95 (3/3.67%)	4147 (3/2.00%)
365 days	19.8 (4/0.33%)	4.12 (8/2.22%)	1.16 (4/5.18%)	4226 (3/0.66%)
Laboratory ambient conditions				
190–210 days	19.5 (17/1.2%)	3.67 (24/6.1%)	1.22 (20/15.0%)	4248 (6/12.4%)

[1]: BS EN 1015-11:1999 - Part 11: Determination of flexural and compressive strength of hardened mortar.
[2]: ASTM C469/C469M-14 [3] Standard Test Method for Static Modulus of Elasticity and Poisson's Ratio of Concrete in Compression.

Table 3
Average mechanical properties accounted for the characterization of simulated historic brick masonry with the adopted NHL mortar, based on mechanical laboratory testing.

Specimens: length × width × height	Material properties			Number of specimens / CoV
Wallets: 625x310x800 [1] (mm^3)	Compressive strength	f_c (MPa)	8.8	4 / 8.3%
	Modulus of elasticity	E (MPa)	909	4 / 6.7%
	Ratio	E/f_c	104.2	4 / 14.5%
Wallets: 625x310x625 [2] (mm^3)	Tensile strength	f_t (MPa)	0.42	3 / 48.7%
	Shear modulus	G (MPa)	485	3 / 33.4%
	Specific weight	ρ (kN/m^3)	18.9	8 / 2.3%
	Ratio	f_t/f_c	0.05	–

[1]: Force control of 1.1 kN/s for cyclic test until $0.7f_c$ and displacement control of 5 μm/s until failure.
[2]: Force control of 0.13 kN/s for cyclic test until $0.7f_t$ and displacement control of 2 μm/s until failure.

normalized average can be used for both rendered and non-rendered wallets.

Prior to the fatigue tests under diagonal compression, the rendered wallets DCf_2, DCf_3 and DCf_4 were subjected to preliminary cyclic diagonal compression testing, with the primary objective to acquire the initial shear stiffness and the diagonal compression capacity ascending envelope. Here, a diagonal compression force of maximum 220 kN was applied, which corresponds to 50% of the tensile strength f_t of the wallet DCf_1 and the complete ascending shear stress–strain envelope was obtained from a linear regression with a least of squares fit and the analytical expression in Hoshikuma et al. [37], here transformed for diagonal compression in Equation (6). Here, the n parameter and the corresponding ratio of the shear modulus G_{mod} to the secant one G_{sec}, was fixed to 2.63 and 1.73 respectively, according to the testing results of DCf_1. As presented in Table 4 and in Fig. 4b, through the fitting process, and before the actual diagonal compression fatigue tests, the initial shear modulus G_{mod} and tensile strength f_t for the wallets DCf_2, DCf_3 and DCf_4, were statistically verified and the normalized shear stress–strain evolution follows the same curvature with the fully tested wallets.

$$f_t = G_{mod}\gamma\left[1-\frac{1}{n}\bullet\left(\frac{\gamma}{\gamma_{ft}}\right)^{n-1}\right], n=\frac{G_{mod}}{G_{mod}-G_{SEC}},\ G_{SEC}=\frac{f_t}{\gamma_{ft}} \tag{6}$$

Diagonal compression fatigue testing of masonry wallets

Equivalent oscillating motion characteristics of a fatigue loading regime under targeted levels of ground-borne vibrations

For an accelerated fatigue experimental test, and according to an exact vibration regime, an equivalent, continuous oscillation is designed, under a constant excitation frequency f. In oscillatory motion, the peak particle velocity (ppv) v is directly linked to the peak particle displacement (ppd) d, the peak particle acceleration (ppa) a, and the vibration frequency f or the radial frequency ω, under the Equation (7), found in BS 5228-2-2009 [9]. The internal motion expression of the displacement $d(x,t)$, under an elastic sinusoidal waveform, is given by Equation (8), with d_o the peak displacement at time zero and k the angular wavenumber of the wave, equal to the ratio of the wave velocity c to the angular frequency ω [33].

$$a = 2\pi fv = (2\pi f)^2 d, \omega = 2\pi f \tag{7}$$

$$d(x,t) = d_o cos(kx - \omega t + \frac{\pi}{2}) \tag{8}$$

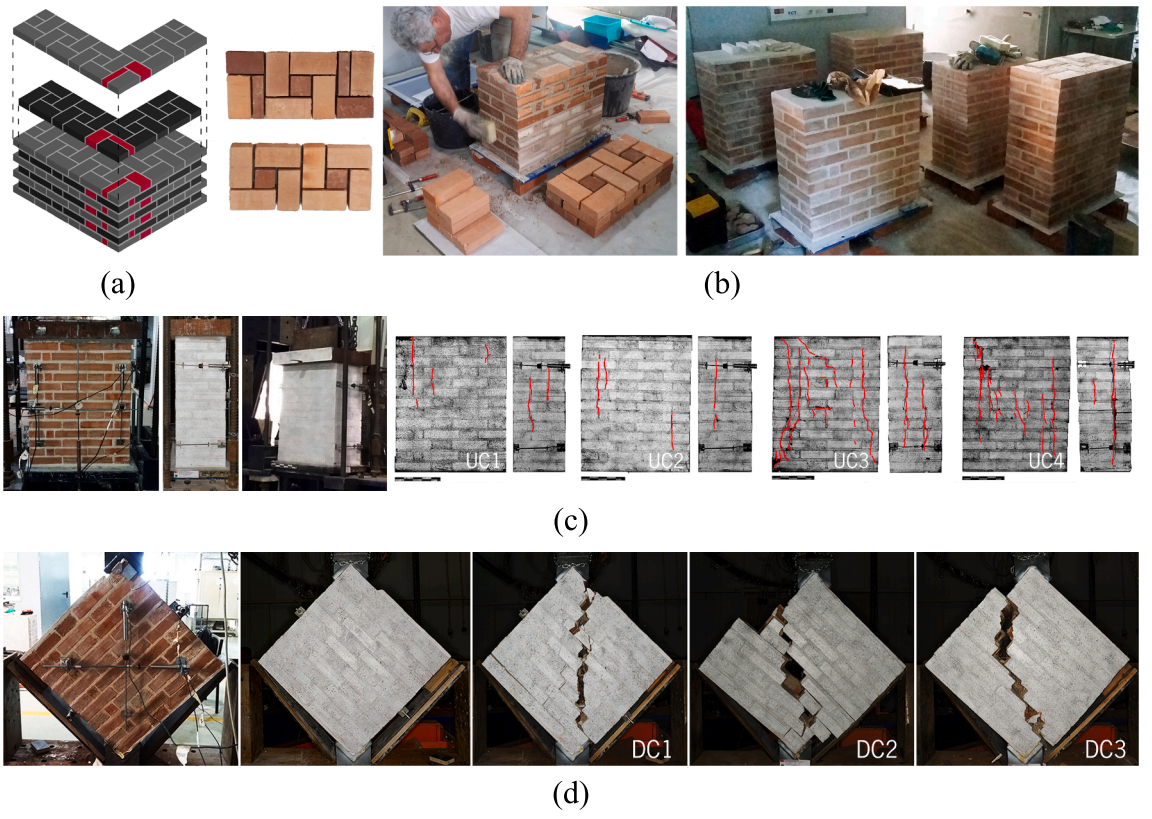

Fig. 2. Replicated historic brick masonry: (a) graphic representation of the Flemish brick bond, at corner interlocking, for 1½ brick of wall thicknesses. Note the cut bricks in red. Adapted from [21] and Lacroux et al. [44]; (b) building process of wallets for uniaxial and diagonal compression tests; geometry, instrumentation and setup of uniaxial (c) and diagonal (d) compression tests on brick masonry wallets, with the resulting crack patterns. (For interpretation of the references to colour in this figure legend, the reader is referred to the web version of this article.)

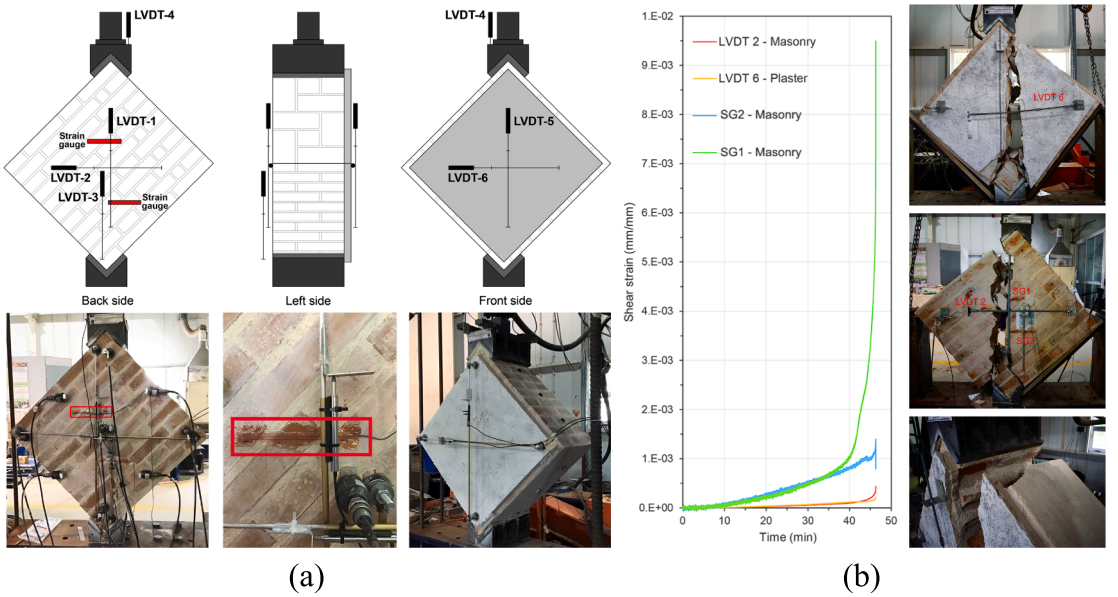

Fig. 3. Diagonal compression cyclic fatigue tests: (a) geometry and instrumentation setup of $DCf_{i\text{-}j}$ wallets; (b) monotonic diagonal compression test of wallet DCf_1, with lateral strains in time, from horizontal LVDTs and SGs, and shear diagonal crack, with splitting of plaster.

Table 4
Evolution of shear loads, shear strain and shear stiffness, during the quasi-static diagonal compression test envelopes of wallets DCf_1, DC_1, DC_2, and DC_3, and envelope curves fits for wallets DCf_2, DCf_3 and DCf_4.

Wallet	%f_t	F	σ_t	$\sigma_{t,norm}$	γ_t	$\gamma_{t,norm}$	G_{sec}	$G_{sec,norm}$	G_{mod}[5]	Goodness of fit[6]
		(kN)	(Mpa)		(mm/mm)		(MPa)		(MPa)	
DCf1[1]	5%f_t	17	0.06	0.05	3.15E-05	0.02	1770	–	1114	SSE
	33%f_t	116	0.37	0.33	3.15E-04	0.21	1180	1.00		9.7E-03
	50%f_t	173	0.56	0.50	4.88E-04	0.32	1143	0.97		R-square / Adj. R-square
	70%f_t	243	0.78	0.70	7.08E-04	0.47	1102	0.93		0.992/0.993
	80%f_t	278	0.89	0.80	8.48E-04	0.56	1051	0.89		RMSE
	90%f_t	312	1.00	0.90	1.02E-03	0.67	984	0.83		34.9E-03
	100%f_t	347	1.11	1.00	1.52E-03	1.00	735	0.62		
DC1[2]	5%f_t	9	0.03	0.05	1.07E-05	0.01	2908	–	1157	SSE
	33%f_t	59	0.21	0.33	1.68E-04	0.16	1269	1.00		2.3E-03
	50%f_t	88	0.32	0.50	2.99E-04	0.28	1071	0.84		R-square / Adj. R-square
	70%f_t	123	0.45	0.70	4.43E-04	0.42	1007	0.79		0.994/0.994
	80%f_t	141	0.51	0.80	5.80E-04	0.55	883	0.70		RMSE
	90%f_t	159	0.58	0.90	7.17E-04	0.68	802	0.63		18.2E-03
	100%f_t	179	0.64	1.00	1.06E-03	1.00	605	0.48		
DC2[2]	5%f_t	4	0.01	0.05	3.06E-05	0.04	405	–	463	SSE
	33%f_t	23	0.08	0.33	1.82E-04	0.22	453	1.00		9.273e-05
	50%f_t	35	0.12	0.50	2.80E-04	0.34	442	0.98		R-square / Adj. R-square
	70%f_t	49	0.17	0.70	3.96E-04	0.48	438	0.97		0.999/0.999
	80%f_t	56	0.20	0.80	4.93E-04	0.60	402	0.89		RMSE
	90%f_t	63	0.22	0.90	5.65E-04	0.69	395	0.87		3.64E-03
	100%f_t	70	0.25	1.00	8.24E-04	1.00	301	0.66		
DC3[2]	5%f_t	5	0.02	0.05	3.71E-05	0.01	4778	–	984	SSE
	33%f_t	33	0.12	0.33	1.06E-04	0.16	1117	1.00		3.7E-03
	50%f_t	50	0.18	0.50	1.59E-04	0.25	1121	1.00		R-square / Adj. R-square
	70%f_t	70	0.25	0.70	2.86E-04	0.44	874	0.78		0.974/0.974
	80%f_t	80	0.29	0.80	3.74E-04	0.58	763	0.68		RMSE
	90%f_t	90	0.32	0.90	4.16E-04	0.64	772	0.69		22.9E-03
	100%f_t	100	0.36	1.00	6.48E-03	1.00	550	0.49		
DCf2[3]	5%f_t	19	0.06	0.05	4.36E-05	0.03	1353	–	**1358**[4]	SSE
	33%f_t	124	0.39	0.33	3.05E-04	0.20	1293	1.00		1.1E-04
	50%f_t	186	0.59	0.50	4.77E-04	0.32	1238	0.96		R-square / Adj. R-square
	70%f_t	261	0.83	0.70	7.21E-04	0.48	1148	0.89		0.999 / 0.998
	80%f_t	298	0.95	0.80	8.69E-04	0.58	1087	0.84		RMSE
	90%f_t	335	1.06	0.90	1.06E-04	0.70	1003	0.78		6.0E-03
	100%f_t	372	**1.18**[4]	1.00	**1.51E-03**[4]	1.00	**784**[4]	0.61		
DCf3[3]	5%f_t	13	0.04	0.05	4.09E-05	0.03	1041	–	**1045**[4]	SSE
	33%f_t	87	0.28	0.33	2.85E-04	0.20	995	1.00		7.5E-05
	50%f_t	131	0.43	0.50	4.47E-04	0.32	953	0.96		R-square / Adj. R-square
	70%f_t	183	0.60	0.70	6.73E-04	0.48	884	0.89		0.999 / 0.999
	80%f_t	209	0.68	0.80	8.15E-04	0.58	836	0.84		RMSE
	90%f_t	235	0.77	0.90	9.94E-04	0.70	771	0.77		3.9E-03
	100%f_t	261	**0.85**[4]	1.00	**1.41E-03**[4]	1.00	**603**[4]	0.61		
DCf4[3]	5%f_t	15	0.05	0.05	4.77E-05	0.03	984	–	**987**[4]	SSE
	33%f_t	97	0.31	0.33	3.33E-04	0.20	940	1.00		2.7E-04
	50%f_t	146	0.47	0.50	5.22E-04	0.32	900	0.96		R-square / Adj. R-square
	70%f_t	204	0.66	0.70	7.86E-04	0.48	835	0.89		0.998 / 0.997
	80%f_t	233	0.75	0.80	9.51E-04	0.58	790	0.84		RMSE
	90%f_t	262	0.85	0.90	1.16E-04	0.70	729	0.77		9.5E-03
	100%f_t	291	**0.94**[4]	1.00	**1.65E-03**[4]	1.00	**570**[4]	0.61		

[1] Displacement control of 2 μm/s.
[2] Force control of 0.13 kN/s for cyclic test until 0.7f_t and displacement control of 2 μm/s until failure.
[3] Force control of 0.13 kN/s for cyclic test until 200 kN.
[4] Predicted material properties, according to the curve fitting process.
[5] Analytical expression in [37], by means of a linear regression with a least of squares fit.
[6] Given early adjustments of the specimen within the testing platens, initial strains until 5% of f_t are not accounted in the fitting process and therefore the shear modulus G_{mod} is accounted for 0–33% of f_t.

For the wallets DCf_i, from the acquired shear force and displacement envelopes of Table 4, fatigue cyclic amplitudes were established, in terms of targeting displacements, and according to the measured stiffness of each wallet. Three ppv thresholds were chosen, one for each of the three tested wallets DCf_i, according to [25]. Considering an average frequency of induced ground-borne vibrations of 65 Hz, as verified through in-situ measurements in Karanikoloudis et al. [41], the ppv values of 8, 10 and 16 mm/s were chosen, which correspond to a lower, an upper bound and a chosen extreme value respectively, for monumental structures with an induced frequency range of 50–100 Hz [25].

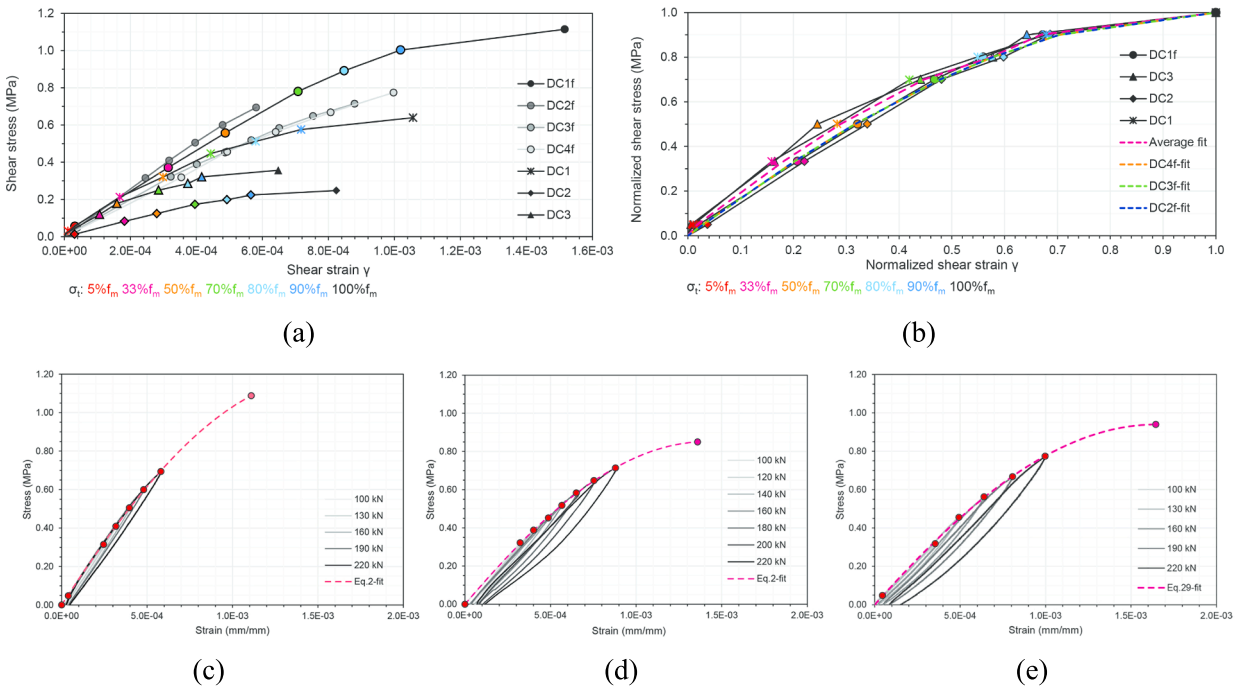

Fig. 4. Diagonal compression tests of DCf_1, DC_1, DC_2, DC_3, DCf_2, DCf_3 and DCf_4: (a) linearized piecewise functions of shear stress–strain curves; (b) normalized shear stress–strain curves until peak and average fit at each designated point. Partial cyclic diagonal compression tests for wallets DCf_2 (c), DCf_3 (d) and DCf_4 (e), with fit envelope curves until peak.

Table 5
Fatigue ppv and ppd target amplitudes, with corresponding force amplitudes.

Specimen DCf_i	Target ppv v_o(mm/s)	Reference dominant radial frequency ω (rad/s)	Reference dominant frequency f (Hz)	Target ppd $d_o = \frac{v_o}{\omega}$(mm)	$K_{chord}^{(100-200)kN}$* (kN/mm)	Target shear force amplitude P_a (kN)
DCf_4	8	408	65	0.018	758.41	14
DCf_2	10			0.025	1113.92	28
DCf_3	16			0.040	771.64	31

* Average chord stiffness from loading and unloading branch.

Following, the ppd values to be applied in the diagonal compression fatigue tests, were defined from the chosen ppv values, according to Equation (7). Hence, in each wallet DCf_i, direct measurements were used from the vertical LVDT 3, attached in masonry and measuring from the center of the diagonal until the lower corner (Fig. 4). From the average chord stiffness, corresponding to a shear force range of 100–200 kN, of the loading and unloading branches of a cyclic static diagonal compression preload test, presented in Fig. 4c, d and e, the diagonal compression amplitude P_a, of the sinusoidal fatigue load, was defined, as shown in Table 5.

Fatigue testing protocols

The fatigue tests in diagonal compression for each wallet DCf_i are defined under a constant shear stress amplitude σ_a, of a cyclic sinusoidal pattern, and at a frequency of 2 Hz. Here is noted that fatigue loading in the laboratory is usually applied as a cyclic quasi-static load, thus, with no dynamic effects. The fatigue tests were divided into static loading A_j, cyclic fatigue loading B_j and static unloading C_j, all under force control, in order to maintain the same stress amplitudes, and monitor shear strain relaxation and stiffness degradation. Considering an average passing train time interval of 4 min and a period of 1.5 years, returns a total of around 150,000 cycles, which according to the assigned cyclic frequency of 2 Hz, the duration of a single fatigue branch B_j was set at around 21 h. Here is noted that static unloading C_j was implemented for each fatigue test j, to avoid the overheating of actuators under long testing durations and also to obtain the reference static stiffness of the subsequent loading part A_{j+1}.

The static shear stress σ_m was considered also a parameter of influence. Initially, an upper bound of 200 kN for the fatigue shear stress σ_{max} is set. Once a fatigue test j is complete without failure (A_j-B_j-C_j), the wallet is loaded at a higher average static shear stress σ_m, with an additional increment of 15 kN ($\simeq 5\%f_t$) and the fatigue test is repeated, until failure is reached. Such a logic can reflect on

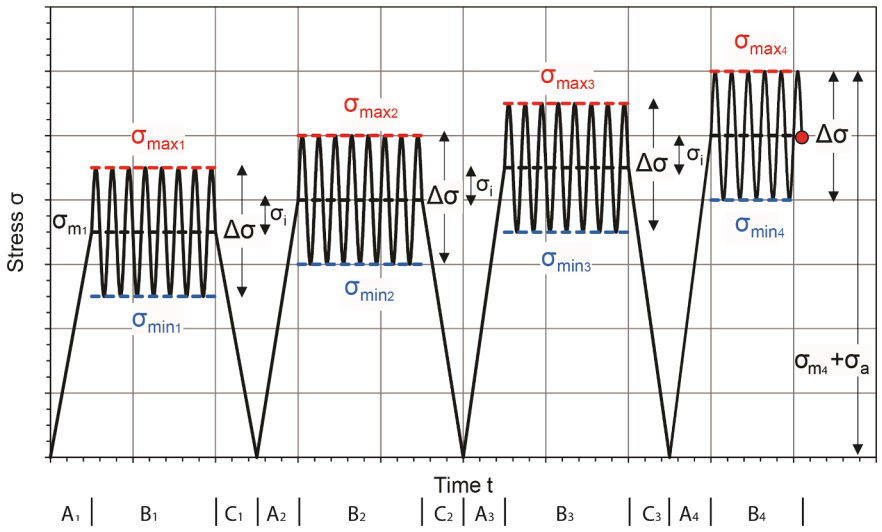

Fig. 5. Loading-fatigue-unloading branches of performed diagonal compression fatigue tests. Note the constant stress range $\Delta\sigma$ and the steady increase of static stress σ_i, until failure.

constant fatigue loading conditions and a static service load increase, i.e., from structural interventions (floor additions, strengthening etc.) and a change of load paths from non-fatigue related damage, namely settlements, earthquakes etc. Here, the details for each fatigue test are presented in Fig. 5 and Table 6.

Instrumentation and data acquisition

By enforcing the testing protocols of Section 3.2 and the fatigue amplitudes of Section 3.1, the accelerated diagonal compression fatigue tests were performed for wallets *DCf*$_2$, *DCf*$_3$ and *DCf*$_4$. In total, acquisitions of diagonal compression fatigue tests, until failure, for each masonry wallet, lasted from 3 to 11 days, with the load-time histories and the failure modes presented in Fig. 6. From Fig. 6b, d and f, it is evident that the resulting failure is the same as the one from the monotonic diagonal compression load application, namely the vertical shear crack at the diagonal, compiled by sliding of bed and head joints, and the splitting of bricks. Regarding the render, it detaches only at the corners, while for the rest of the wall, it follows the same split throughout. For wallet *DCf*$_3$, a double vertical fragmentation occurs, forming a somewhat diagonal pole (Fig. 6f).

The sequential process of the diagonal compression fatigue tests for all three wallets, together with shear stiffness acquired data at the beginning and end of the fatigue test, are presented in Table 7. According to the fatigue loading regimes, the *DCf*$_2$ wallet was subjected to 11 fatigue tests (*ppv* = 10 mm/s, $\sigma_a = 0.09$ MPa and $\sigma_m = 0.59$–0.94 MPa), the wallet *DCf*$_3$ to 3 fatigue tests (*ppv* = 16 mm/s, $\sigma_a = 0.1$ MPa and $\sigma_m = 0.54$–0.64 MPa), and the wallet *DCf*$_4$ to 6 fatigue tests (*ppv* = 8 mm/s, $\sigma_a = 0.04$ MPa and $\sigma_m = 0.60$–0.84 MPa). Here is noted that for the first tested specimen *DCf*$_2$, four initial and identical consecutive fatigue stress combinations were chosen in order to verify the evolution state of stiffness degradation and strain relaxation for a larger time span.

Fatigue data under temperature effect and displacement compensation

The fatigue tests were performed in a conventional steel testing frame within a closed laboratory, without controlled environmental conditions. Hence, displacement data being temperature dependent, followed complex contractions and dilations, from the masonry wallets and the metallic rods of the LVDTs. In fact, from a 48 h acquisition in one of the wallets, without load application, the measured dilations and contractions, are in a somewhat linear trend with the temperature from a sensor, placed next to the wallet (Fig. 7a). Thus, temperature sensors provided continuous readings throughout the fatigue tests, and the linear temperature effects were compensated,

Table 6
Fatigue testing protocols for the three consecutive loading branches.

Loading branch	A_j	B_j	C_j
Load Pattern	Monotonic	Sinusoidal	Monotonic
Control type	Force	Force	Force
Loading rate	0.12 kN/s	2 Hz	0.12 kN/s
Sampling rate	4 Hz	25 Hz	2 Hz
Recording	Continuous	5 Cycles/100 s	Continuous
Safety condition	Relative displacement of 25 mm		
Cycles	1	150,000	1

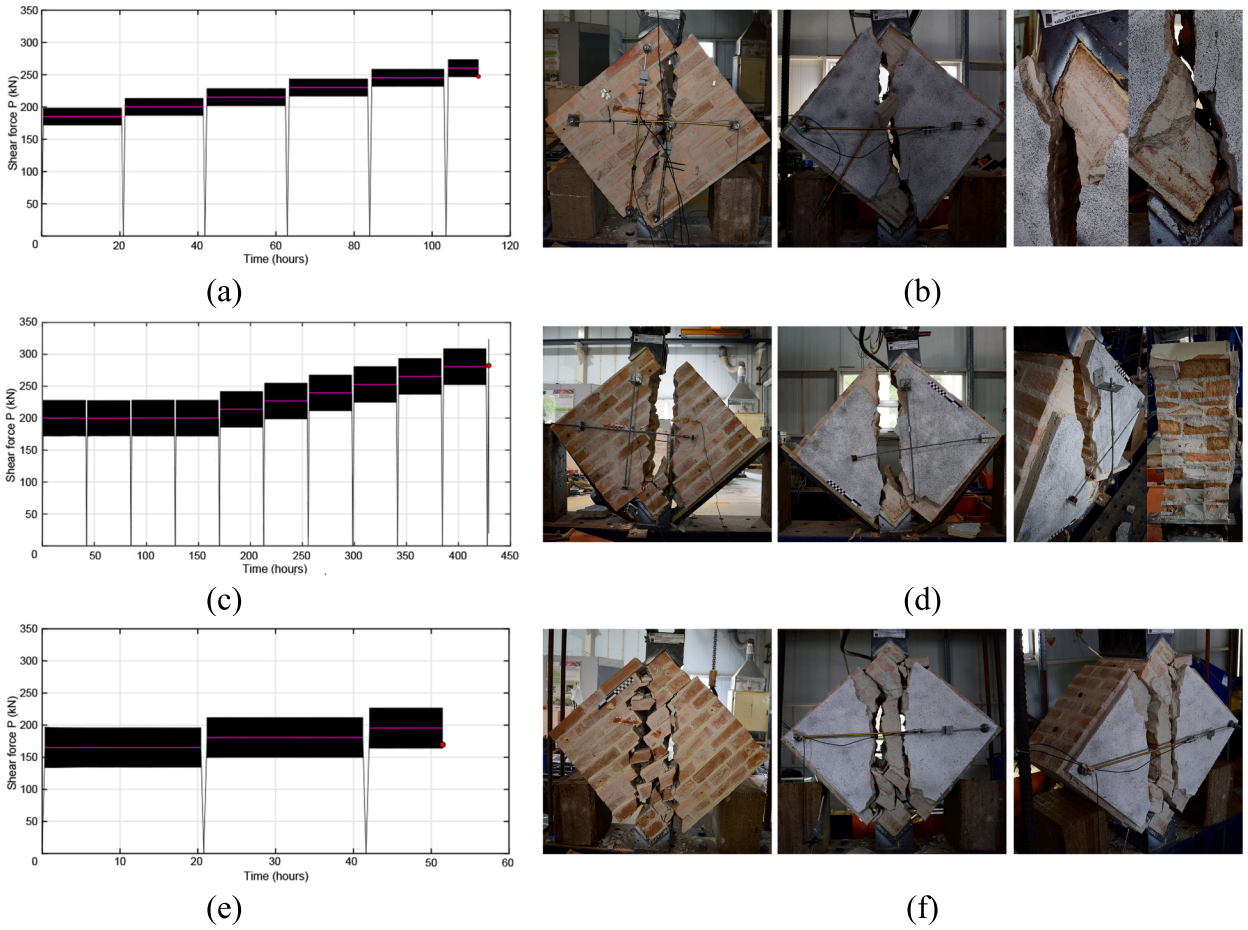

Fig. 6. Diagonal compression fatigue load-time histories for wallets DCf_4 (a), DCf_2 (c) and DCf_3 (e), and respective failure modes (b), (d) and (f).

while for the loading and unloading branches, those were found insignificant.

The process of temperature compensation, for the strains from the LVDTs and the SGs, for every fatigue branch *j* of each wallet DCf_i, had to follow an initial stage of resampling, through linear interpolating functions, to match the sampling rates. Here, the average direct displacements were obtained from the upper and lower envelops and the entire process of temperature compensation is visualized in the diagram of Fig. 7b. The translation-temperature correlation differs between each fatigue branch, attributed to the compilation of the many dilating and contracting elements. A limit was established, for accounting the temperature effects, namely an R-square value of the linear trendline higher than 0.7. As fatigue cycles progressed, where strains also increased, temperature effects were found less significant.

Resulting strain–time histories in the masonry and render of wallets DCf_i, with temperature compensation, are presented in Fig. 8, Fig. 9 and Fig. 10. Direct average shear strains in masonry exhibit small but positive trends, while in the render are also found increasing, but less in amplitude, attributed to the uneven sectional stiffness of the wallet. At the last fatigue branch, and before failure, in wallets DCf_3 and DCf_4, the diagonal compression strains in the render are diminishing, which indicates that the render is under a reversed mostly vertical deformation, due to out-of-plane bending and bulging (Fig. 8 and Fig. 10).

Regarding the SGs attached in masonry, their use appears particularly beneficial, as they can capture fatigue strain reversals, with positive or negative trends. As seen in Fig. 9 and Fig. 10, for the strain gauges that cover the crack area, as in wallet DCf_3 and DCf_2, the acquired lateral fatigue strains increase exponentially, until failure.

Experimental results on fatigue shear

Cyclic loading and stiffness monitoring

For the diagonal compression fatigue tests in wallets $DCf_{i\text{-}j}$, under different static diagonal compression stresses and fatigue amplitudes, average shear strains and secant shear stiffness time-histories were obtained, from the upper and lower bound envelopes. Initially, the secant shear stiffness at the end of each static A_j and fatigue branch B_j are compared, and the respective values, for each

Table 7
Fatigue variables for diagonal compression, for each of the testing wallets $DCf_{i\text{-}j}$.

	A_i		**B_i**						**C_i**		**A_{i+1}**	
$DCf_{i,j}$	Peak shear load P_m kN	Peak shear load σ_m mPa/%f_t*	Shear load range P_a kN	Shear stress range σ_a MPa/%f_t*	R $\left(\frac{\sigma_{min}}{\sigma_{max}}\right)$	A $\left(\frac{\sigma_a}{\sigma_m}\right)$	S $\left(\frac{\sigma_{max}}{\sigma_m}\right)$	Cycles	Peak shear load P_m kN	Peak shear stress σ_m MPa/%f_t*	Shear force incr. P_i kN	Shear stress incr. σ_i MPa/%f_t*
$DCf_{2\text{-}1}$	200	0.59/50%	28	0.09/8%	0.74	0.15	1.15	$1.5{\cdot}10^5$	200	0.59/50%	–	–
$DCf_{2\text{-}2}$	200	0.59/50%	28	0.09/8%	0.74	0.15	1.15	$1.5{\cdot}10^5$	200	0.59/50%	–	–
$DCf_{2\text{-}3}$	200	0.59/50%	28	0.09/8%	0.74	0.15	1.15	$1.5{\cdot}10^5$	200	0.59/50%	–	–
$DCf_{2\text{-}4}$	200	0.59/50%	28	0.09/8%	0.74	0.15	1.15	$1.5{\cdot}10^5$	200	0.59/50%	–	–
$DCf_{2\text{-}5}$	215	0.64/54%	28	0.09/8%	0.75	0.14	1.14	$1.5{\cdot}10^5$	215	0.64/54%	15	0.05/4%
$DCf_{2\text{-}6}$	220	0.69/58%	28	0.09/8%	0.77	0.13	1.13	$1.5{\cdot}10^5$	220	0.69/58%	15	0.05/4%
$DCf_{2\text{-}7}$	235	0.74/63%	28	0.09/8%	0.78	0.12	1.12	$1.5{\cdot}10^5$	235	0.74/63%	15	0.05/4%
$DCf_{2\text{-}8}$	250	0.79/67%	28	0.09/8%	0.80	0.11	1.11	$1.5{\cdot}10^5$	250	0.79/67%	15	0.05/4%
$DCf_{2\text{-}9}$	265	0.84/71%	28	0.09/8%	0.81	0.11	1.11	$1.5{\cdot}10^5$	265	0.84/71%	15	0.05/4%
$DCf_{2\text{-}10}$	280	0.89/75%	28	0.09/8%	0.82	0.10	1.10	$1.5{\cdot}10^5$	280	0.89/75%	15	0.05/4%
$DCf_{2\text{-}11}$	295	0.94/79%	28	0.09/8%	0.83	0.10	1.10	4**	295	0.94/79%	15	0.05/4%
$DCf_{3\text{-}1}$	165	0.54/63%	31	0.10/12%	0.64	0.22	1.22	$1.5{\cdot}10^5$	165	0.54/63%	–	–
$DCf_{3\text{-}2}$	180	0.59/69%	31	0.10/12%	0.66	0.20	1.20	$1.5{\cdot}10^5$	180	0.59/69%	15	0.05/6%
$DCf_{3\text{-}3}$	195	0.64/75%	31	0.10/12%	0.68	0.19	1.19	$7.0{\cdot}10^4$**	195	0.64/75%	15	0.05/6%
$DCf_{4\text{-}1}$	185	0.60/64%	14	0.04/4%	0.88	0.07	1.07	$1.5{\cdot}10^5$	185	0.60/64%	–	–
$DCf_{4\text{-}2}$	200	0.65/69%	14	0.04/4%	0.88	0.06	1.06	$1.5{\cdot}10^5$	200	0.65/69%	15	0.05/5%
$DCf_{4\text{-}3}$	215	0.69/73%	14	0.04/4%	0.89	0.06	1.06	$1.5{\cdot}10^5$	215	0.69/73%	15	0.05/5%
$DCf_{4\text{-}4}$	230	0.74/79%	14	0.04/4%	0.90	0.05	1.05	$1.5{\cdot}10^5$	230	0.74/79%	15	0.05/5%
$DCf_{5\text{-}5}$	245	0.79/84%	14	0.04/4%	0.90	0.05	1.05	$1.5{\cdot}10^5$	245	0.79/84%	15	0.05/5%
$DCf_{4\text{-}6}$	260	0.84/89%	14	0.04/4%	0.91	0.05	1.05	$6.3{\cdot}10^4$**	260	0.84/89%	15	0.05/5%

* Estimated diagonal compression monotonic capacity, from fitting cyclic preload tests with Equation (6).
** Number of cycles before failure.

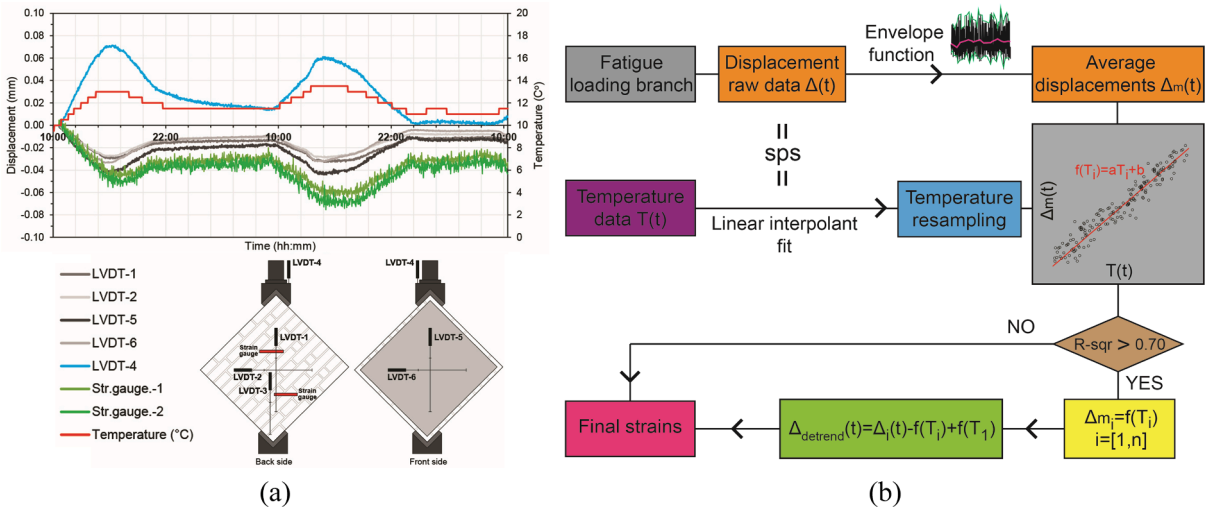

Fig. 7. Temperature variations in displacement acquisition data for testing conditions of DCf_i wallets: (a) displacement and temperature time histories from respective LVDTs, SGs and temperature sensors for a 48 h recording period, without external loading; (b) process diagram for temperature compensation for fatigue displacement raw data.

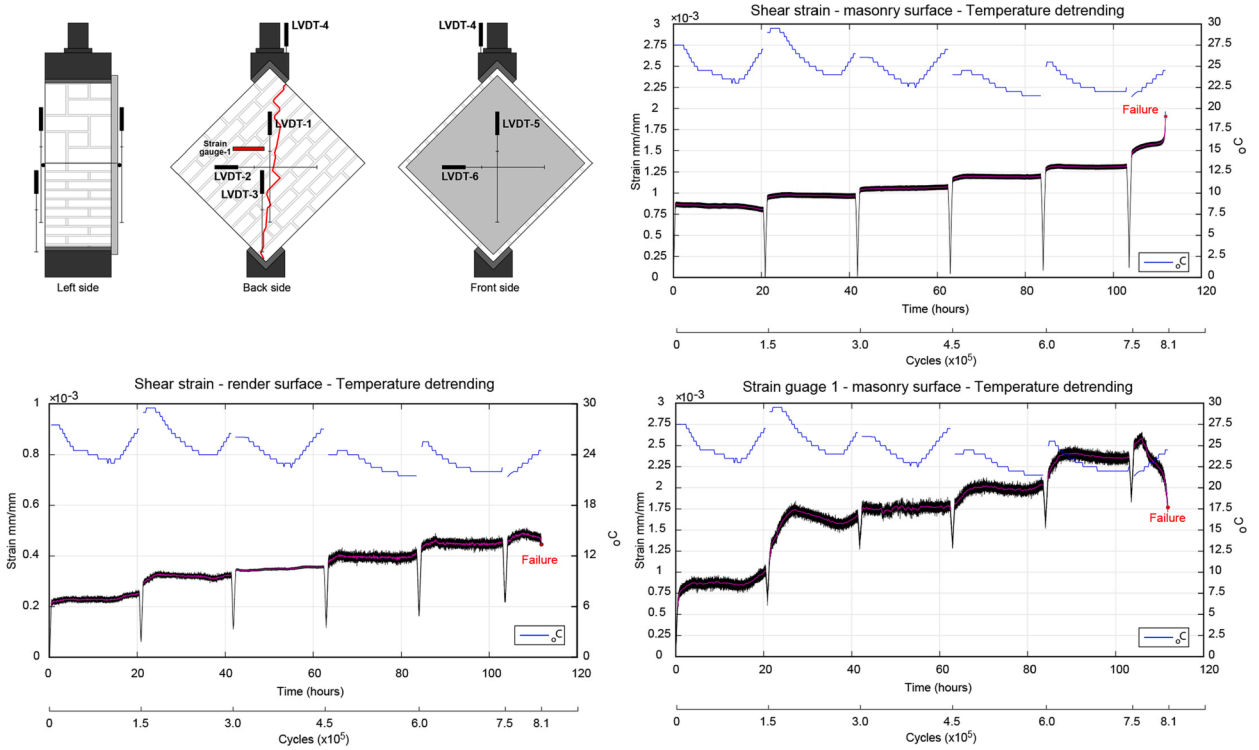

Fig. 8. Temperature detrending of fatigue cyclic shear tests in diagonal compression for wallet DCf_4, with strain–time histories in the masonry and render from LVDTs and SGs. Note the temperature evolution, the failure point and average fatigue strain in magenta. (For interpretation of the references to colour in this figure legend, the reader is referred to the web version of this article.)

wallet $DCf_{i\text{-}j}$ are presented in Table 8, Table 9 and Table 10. Values of the secant shear stiffness pose an evident decrease after each fatigue branch B_j, which for fatigue loads not leading to failure ranges between 3 and 17%, with a somewhat steady decrease, at the gradual increase in static loading, but also at the constant static loading of the $DCf_{2\text{-}(1-4)}$ fatigue branches. Yet, for the $DCf_{3\text{-}3}$ and $DCf_{4\text{-}6}$ fatigue branches, where fatigue failure occurs, the relative decrease in the secant shear stiffness reaches 59% and 27% respectively.

By considering the distinctive fatigue stages leading to failure, for $DCf_{3\text{-}3}$ the shear stiffness decrease concurs to 22% for Stage I (0–10%N_f), 20% for Stage II (10–80%N_f) and 58% for Stage III (80–100%N_f). Similarly, for $DCf_{4\text{-}6}$ the shear stiffness decrease

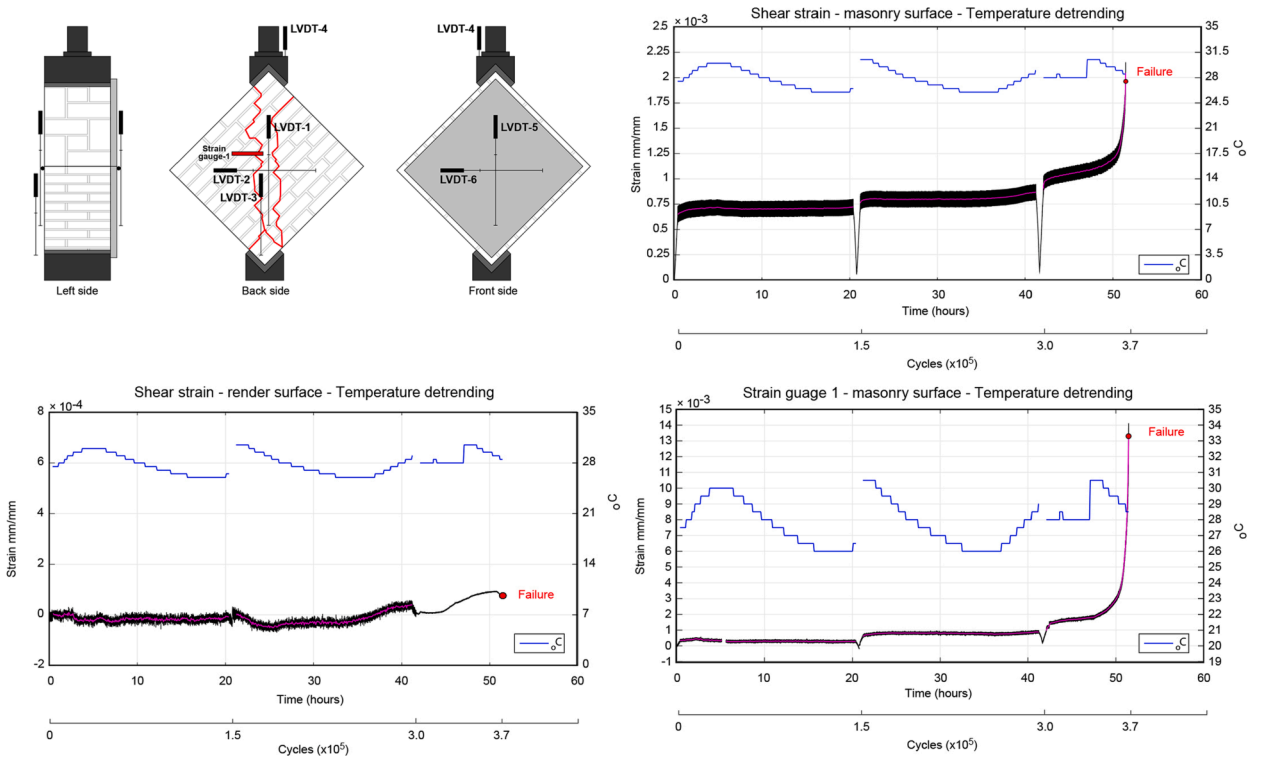

Fig. 9. Temperature detrending of fatigue cyclic shear tests in diagonal compression for wallet DCf_3, with strain–time histories in the masonry and render from LVDTs and SGs. Note the temperature evolution, the failure point and average fatigue strain in magenta. (For interpretation of the references to colour in this figure legend, the reader is referred to the web version of this article.)

corresponds to 18% for Stage I (0–10%N_f), 19% for Stage II (10–80%N_f) and 63% for Stage III (80–100%N_f). Considering the maximum shear stress σ_{max} of the last fatigue branch, both specimens DCf_3 and DCf_4 appear to have crossed the static stress limit for macrocracks, which according to Brooks [8] is set at $0.7f_t$, while for $DCf_{4\text{-}6}$ σ_{max} is in fact placed in the last shear stress area of unstable crack-growth ($>0.9f_t$). Also, the elastic shear modulus is diminishing gradually, after each fatigue branch, with the highest difference at the last loading branch before failure. Here is noted that for the last fatigue test of $DCf_{2\text{-}11}$ no shear stiffness decrease could be captured, considering that the specimen failed after only four cycles.

Following, for each tested wallets DCf_i, since fatigue was accessed under various diagonal compression static stress $\sigma_{m,i\text{-}j}$ and fatigue stress rates $\sigma_{a,i\text{-}j}$, and under a constant number of cycles, i.e., $1.5x10^5$ cycles, shear strain quantities from each fatigue branch were considered as independent, with the ones leading to failure acknowledged as a complete fatigue test. Thus, average secant shear stiffness evolution graphs, for each fatigue branch B_j, and each masonry wallet $DCf_{i\text{-}j}$, were normalized to the initial values from the first static loading branch A_1 and presented in Fig. 11a, Fig. 12a and Fig. 13a, superposed with shear stress–strain curves. During the progression of fatigue tests B_j, strain relaxation increases, while the secant shear stiffness is diminishing exponentially, with respect to shear strain, as fatigue tests progress.

Next, accounting for the shear strain and secant shear stiffness, during each fatigue loading branch B_j for all three wallets DCf_i, their evolution with respect to the number of cycles is presented in Fig. 11b and c, Fig. 12b and c and Fig. 13b and c. After each consecutive series of loading-fatigue-unloading branches A_j-B_j-C_j, residual-irrecoverable or else plastic strains increase in amplitude and progress under a small but positive slope, being partly the result of fatigue, and partly from the cyclic progression of the static shear stresses.

In addition, the evolution rates of the mean, fatigue shear strains and the secant shear stiffness are computed as the first derivatives with respect to the number of cycles N_i, with the latter transformed in an equivalent numeric array, of 12 increments per cycle, following the sampling frequency of the fatigue data. Further on, continuous average shear strain and shear secant stiffness time-cycle series were obtained, with linear interpolation functions. Since real time-history data are abrupt and noisy, their first derivative in time can be highly unreliable, with extreme peaks and offsets. Hence, in order to obtain smooth time rates, time series were fitted into a 9th order polynomial and subsequently differentiated (Fig. 11d and e, Fig. 12d and e and Fig. 13d and e). As recorded, the shear strain and secant shear stiffness rates, after the initial large rates of Stage I, in many tests they do not present a stable linear slope, instead they vary fluctuating, which can be explained by the diversion of load paths, as cracks progress.

Next, the focus is set on the rates of fatigue Stage II, which for each fatigue loading branch B_j wallet DCf_i are presented in Table 11. For a complete fatigue test, resulting in failure, Stage II corresponds to the range of 10–80% of N_f. Yet, for fatigue tests with no failure, the average shear strain and secant shear stiffness rates of fatigue Stage II, were considered for 30–100% of the applied cycles. Fatigue branches under increasing static diagonal compression, exhibit growing and decaying rates, regarding the mean shear strains and

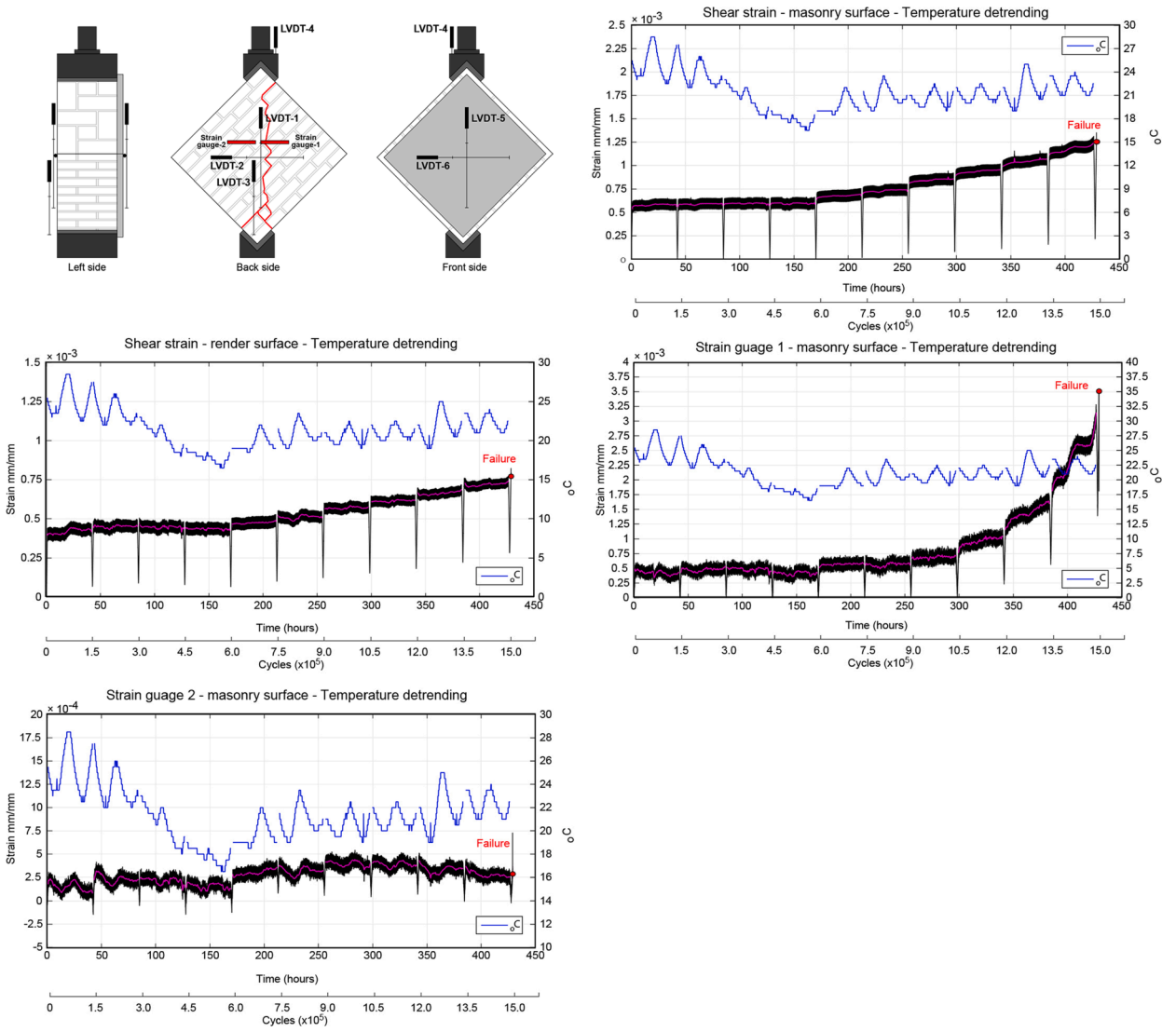

Fig. 10. Temperature detrending of fatigue cyclic shear tests in diagonal compression for wallet DCf_2, with strain–time histories in the masonry and render from LVDTs and SGs. Note the temperature evolution, the failure point and average fatigue strain in magenta. (For interpretation of the references to colour in this figure legend, the reader is referred to the web version of this article.)

Table 8
Shear stiffness evolution during static A_j and fatigue B_j branches, for wallet DCf_2.

DCf2-j($\sigma_{m,2\text{-}j}$*,±$\sigma_{a,2\text{-}j}$*)	Cycles**	ΔG_{sec} ($B_{j,10\%}$-A_j)	ΔG_{sec} ($B_{j,100\%}$-A_j)	ΔG_{mod} (A_j-A_1)
DCf2-1(0.50f_t,±0.08f_t)	1.50E + 05	−6%	−9%	0%
DCf2-2(0.50f_t,±0.08f_t)	3.00E + 05	−4%	−7%	−5%
DCf2-3(0.50f_t,±0.08f_t)	4.50E + 05	−3%	−4%	−9%
DCf2-4(0.50f_t,±0.08f_t)	6.00E + 05	−3%	−5%	−8%
DCf2-5(0.54f_t,±0.08f_t)	7.50E + 05	−5%	−10%	−10%
DCf2-6(0.58f_t,±0.08f_t)	9.00E + 05	−4%	−8%	−12%
DCf2-7(0.63f_t,±0.08f_t)	1.05E + 06	−4%	−7%	−16%
DCf2-8(0.67f_t,±0.08f_t)	1.20E + 06	−5%	−9%	−18%
DCf2-9(0.71f_t,±0.08f_t)	1.35E + 06	−5%	−10%	−19%
DCf2-10(0.75f_t,±0.08f_t)	1.50E + 06	−4%	−14%	−22%
DCf2-11(0.79f_t,±0.08f_t)	1.50E + 06	–	–	−28%

* Stated as a ratio of f_t, with f_t estimated according to Section 2.3.
** Counting from the beginning of the fatigue tests, presented as a sum.

Table 9
Shear stiffness evolution during static A_j and fatigue B_j branches, for wallet DCf_3.

DCf3-j($\sigma_{m,3\text{-}j}$*,$\pm\sigma_{a,3\text{-}j}$*)	Cycles**	ΔG_{sec} ($B_{j,10\%}$-A_j)	ΔG_{sec} (A_j-$B_{j,80\%}$)	ΔG_{sec} $B_{j,100\%}$-A_j)	ΔG_{mod} (A_j-A_1)
DCf3-1(0.54f_t,±0.12f_t)	1.50E + 05	−14%	–	−16%	0%
DCf3-2(0.59f_t,±0.12f_t)	3.00E + 05	−11%	–	−17%	−2%
DCf3-3(0.64f_t,±0.12f_t)	3.70E + 05	−13%	−25%	−59%	−14%

* Stated as a ratio of f_t, with f_t estimated according to Section 2.3.
** Counting from the beginning of the fatigue tests, presented as a sum.

Table 10
Shear stiffness evolution during static A_j and fatigue B_j branches, for wallet DCf_4.

DCf4-j($\sigma_{m,4\text{-}j}$*,$\pm\sigma_{a,4\text{-}j}$*)	Cycles**	ΔG_{sec} ($B_{j,10\%}$-A_j)	ΔG_{sec} (A_j-$B_{j,80\%}$)	ΔG_{sec} ($B_{j,100\%}$-A_j)	ΔG_{mod} (A_j-A_1)
DCf4-1(0.64ft,±0.04ft)	1.50E + 05	−3%	–	3%	0%
DCf4-2(0.69ft,±0.04ft)	3.00E + 05	−6%	–	−5%	−5%
DCf4-3(0.73ft,±0.04ft)	4.50E + 05	−5%	–	−7%	−8%
DCf4-4(0.79ft,±0.04ft)	6.00E + 05	−6%	–	−6%	−12%
DCf4-5(0.84ft,±0.04ft)	7.50E + 05	−5%	–	−6%	−15%
DCf4-6(0.89ft,±0.04ft)	8.13E + 05	−5%	−10%	−27%	–23%

* Stated as a ratio of f_t, with f_t estimated according to Section 2.3.
** Counting from the beginning of the fatigue tests, presented as a sum.

mean shear secant stiffness respectively, indicative of fatigue damage, through the formation of microcracks, the transition to macrocracks and concluding to failure. In wallet DCf_2, shear strain rates for fatigue branches $DCf_{2\text{-}1}$ until $DCf_{2\text{-}5}$ ($S = 1.15$–1.14) are found somewhat stable, while the rest are increasing until the last fatigue branch of $DCf_{2\text{-}10}$, reaching the highest shear strain rate of 4.5E-11. Further on, in wallet DCf_3, and given the higher fatigue rates ($S = 1.22$–1.19), shear strain rates are found increasing for each consecutive fatigue branch, reaching the highest values of 2.8E-10. The wallet DCf_4, being subjected to the lower shear stress rates of fatigue ($S = 1.07$–1.05), exhibits positive shear strain rates from the fatigue branch $DCf_{4\text{-}3}$, which keep increasing until the value of 1.5E-10, measured during the Stage II fatigue branch of $DCf_{4\text{-}6}$. Thus, higher shear strain rates of fatigue Stage II, are found for higher static shear stresses. As far as the cyclic rates of the secant shear stiffness are concerned, those are diminishing during each fatigue branch, with the highest decay within the range of 4.0E-05 to 1.9E-04.

Lastly, the correlation between the secant shear stiffness and the shear strain from all fatigue tests of $DCf_{2\text{-}j}$, $DCf_{3\text{-}j}$ and $DCf_{4\text{-}j}$, normalized with respect to the secant shear stiffness of the preceding loading branch and the shear strain at the last step of each fatigue branch, is visualized graphically in Fig. 14. Here is noted that $DCf_{3\text{-}3}$ and $DCf_{4\text{-}6}$ are considered as complete fatigue tests, with the maximum recorded shear strain and final secant shear stiffness corresponding to the ones before failure.

The secant shear stiffness and shear strain decay were fitted to an exponential equation under a reverse power law, given in Equation (9). Here, the b exponent is the order of scaling, which for tests $DCf_{2\text{-}(1\text{-}6)}$, $DCf_{3\text{-}1}$ and $DCf_{4\text{-}(1\text{-}4)}$ not leading to failure is almost equal to −1, meaning that the normalized shear strain and secant shear stiffness present an almost linear, but reverse correlation. Instead, for tests $DCf_{2\text{-}(7\text{-}10)}$, $DCf_{3\text{-}(2\text{-}3)}$ and $DCf_{4\text{-}(5\text{-}6)}$ the fitted order of scaling b is within the range of −1.1 to −1.2, which is indeed exponential and indicative of fatigue advanced crack propagation, with the shear strain exhibiting slightly higher rates of deterioration compared to those for secant shear stiffness degradation. The d constant corresponds to the final value of the normalized secant shear stiffness before failure or at the last documented step.

$$\frac{G_{sec,Ni}}{G_{sec,Aj,last}} = d\left(\frac{\gamma_{t,Ni}}{\gamma_{t,N_{last}}}\right)^{b}, d > 0 \; and \; b < 0 \tag{9}$$

Analytical shear stress–strain interpretations and correlations

Regarding the three stages of a complete fatigue test, resulting to failure, the average, fatigue shear strain and secant shear stiffness evolution, with respect to the number of cycles N_i, resembles a reverse, non-symmetric S-shaped curve, with a zero and a maximum asymptote, and a known cycle size N_f, i.e., a Gompertz curve, given by Equation (10) [40]. Here p, g and h are positive coefficients. Transforming the Equation (10) into a reverse form, with the y and × variables representing the fatigue cycles N_i and the average shear strain γ_t or secant shear stiffness G_{sec} respectively, the reversed non-symmetrical sigmoid functions of the Gompertz equation are presented in Equation (11) and Equation (12). For the shear secant stiffness sigmoid fit, a negative sign and a fourth coefficient q are considered, in order to accommodate the inverted N_i axis and the offset from zero respectively. In physical terms, the p coefficient is equal to the number of fatigue cycles leading to failure N_f, the g coefficient controls the deflection point of the curve, and the h coefficient represents the scale of the shear strains and secant shear stiffness. By means of minimizing the sum of square errors, the resulted analytical curves of the fatigue branches $DCf_{3\text{-}3}$ and $DCf_{4\text{-}6}$, with R-squared values higher than 0.90, are presented in Fig. 15. Yet, a larger number of fatigue tests are needed, in order to establish relative correlations with static shear properties and fatigue shear rates.

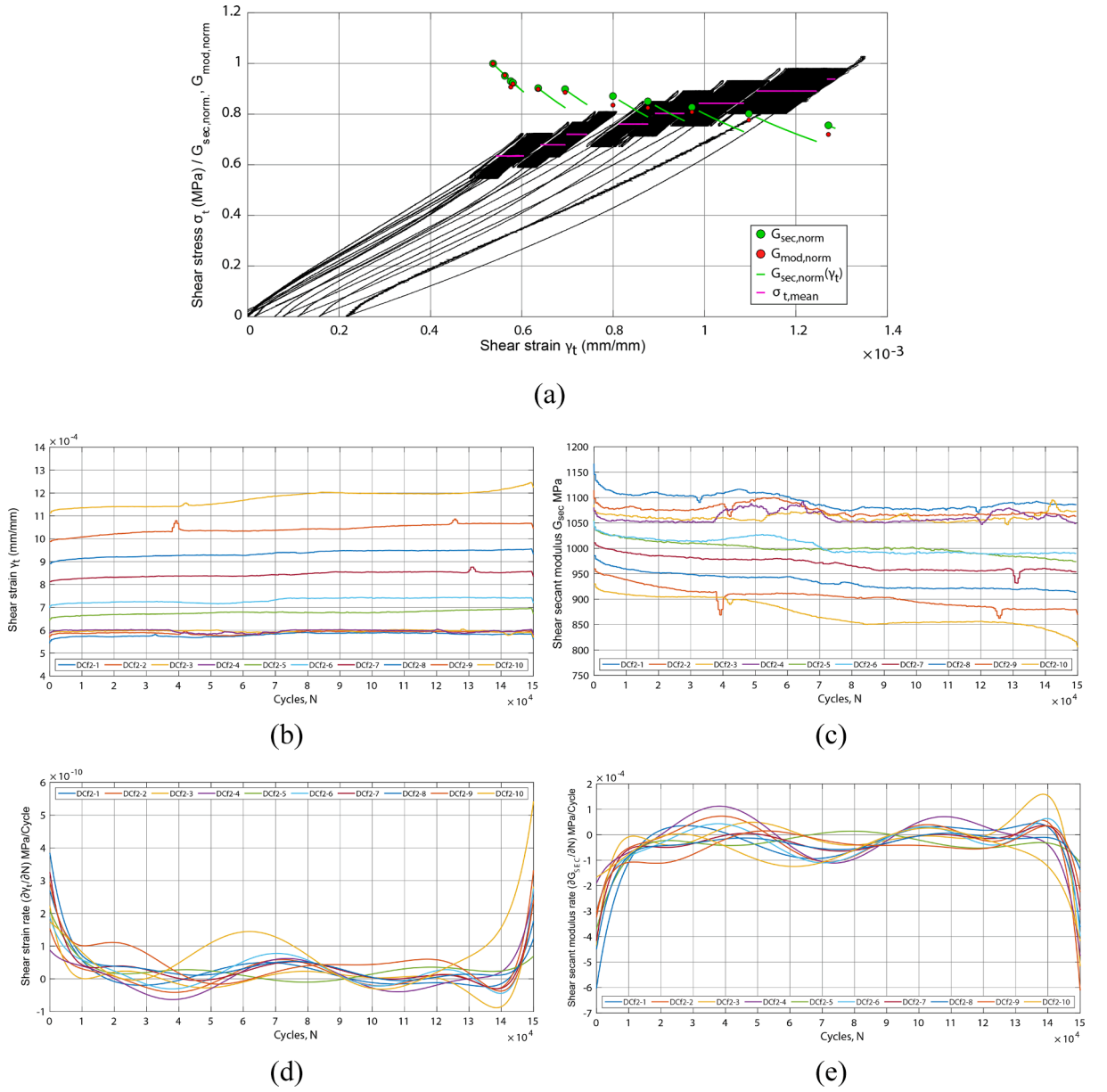

Fig. 11. Fatigue acquisition data, for wallet DCf_2 in diagonal compression: (a) shear stress–strain curve in masonry surface, with the shear elastic and secant modulus, normalized to the initial respective values; average shear strain (b) and secant shear stiffness evolution (c), and their respective rates (d) and (e), with respect to fatigue cycles N.

$$y(x) = e^{p - ge^{-hx}} \tag{10}$$

$$\gamma_t(N_i) = \frac{g - ln(ln(p/N_i))}{h} \tag{11}$$

$$G_{sec}(N_i) = q - \frac{g - ln(ln(p/N_i))}{h} \tag{12}$$

In order to conduct a fatigue life-estimate assessment, under a specific static and fatigue stress regime, and before failure is reached, the hypothesis of Holmen [36] of equal fatigue failure properties is used, namely the maximum shear strain $\gamma_{t,\max}(N_f)$. Considering an end-to-end linear piecewise function for the normalized secant shear stiffness curve, with respect to the normalized fatigue cycles N_i, the decaying linear curve, for each of the wallets $DCf_{3\text{-}3}$ and $DCf_{4\text{-}6}$ is given by 13 and Fig. 16, where λ is slope of the end-to-end piecewise linear functions. Thus, under the hypothesis of constant fatigue failure properties, the estimated fatigue life of the

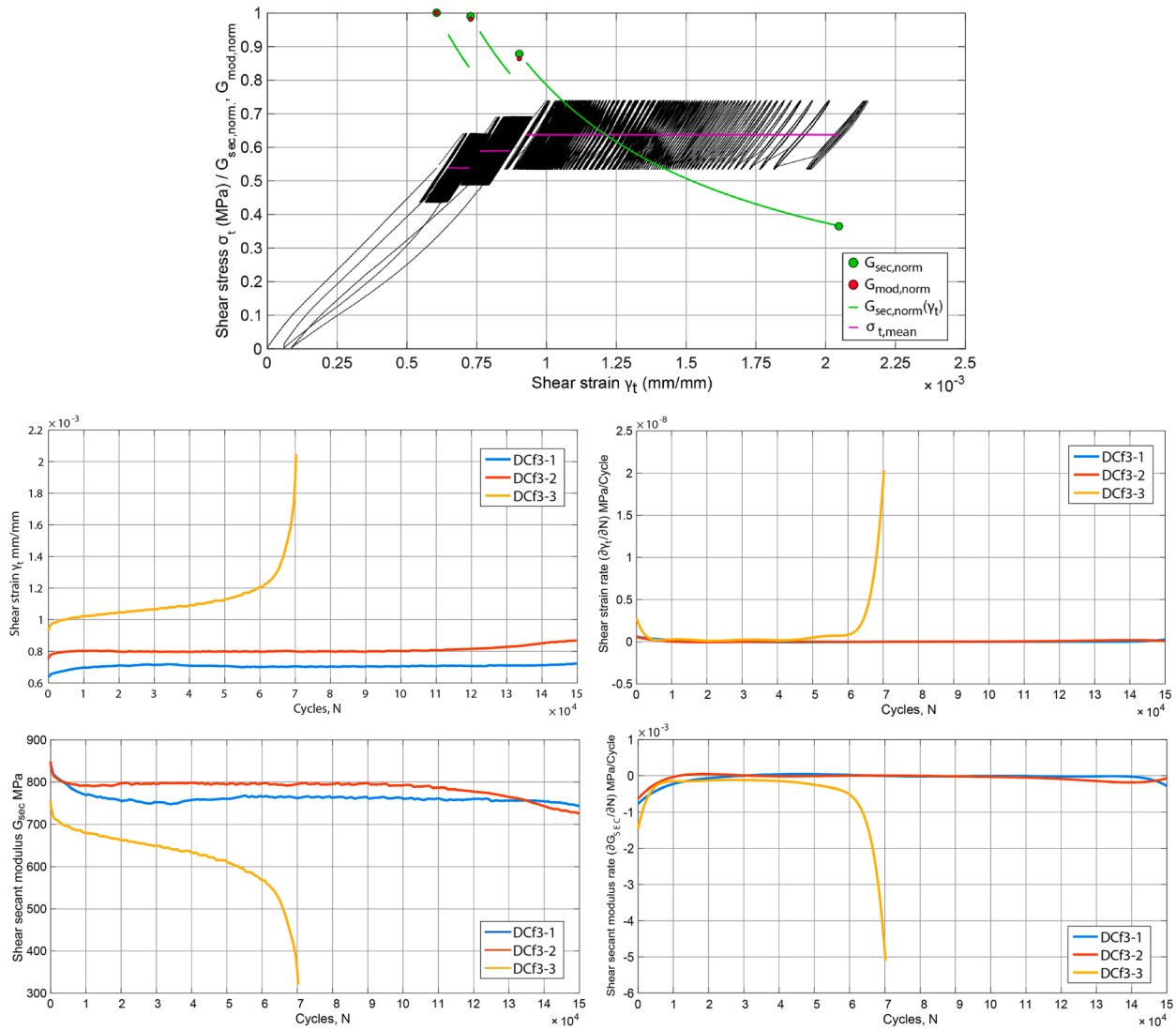

Fig. 12. Fatigue acquisition data, for wallet DCf_3 in diagonal compression: (a) shear stress–strain curve in masonry surface, with the shear elastic and secant modulus, normalized to the initial respective values; average shear strain (b) and secant shear stiffness evolution (c), and their respective rates (d) and (e), with respect to fatigue cycles N.

various, preceding fatigue stress states, without failure is presented in Table 12. Here, the estimated fatigue lives for $DCf_{3\text{-}(1-5)}$ and $DCf_{4\text{-}(1-2)}$, are higher by one and two orders of magnitude respectively, compared to the actual fatigue branches resulting in failure.

$$\frac{G_{sec,N_i}}{G_{sec,N=1}} = 1 - \lambda \frac{N_i}{N_f} \tag{13}$$

Discussion and technical recommendations

The philosophy of design building codes, accounts for the nature of the loading regime, namely static, dynamic, creep, fatigue etc., which can potentially decay stiffness and capacity, and thus, a reduction coefficient is assigned for the material properties. E.g., in EN 1992.1.1:2004 [28], and for the ULS, a coefficient equal to 1.8 is found, accounting for the nominal strength, which is considered in line with the outcomes of the conducted fatigue tests in masonry wallets. Besides, the process of structural assessment in cultural heritage buildings should also include fatigue reduction coefficients, similarly to the assessment for creep, accounting for the stiffness degradation in masonry, e.g., in EN 1996:2005 [30]. Thus, considering the maximum decay in the values of shear modulus found in this work, a fatigue overall reduction coefficient, for the nominal shear modulus in the range of 1.5, applies.

Accounting for field monitoring aspects, within the process of fatigue assessment in masonry historic structures, first, a long-term monitoring process should conclude on the amplitude, frequency and spatial distribution of ground-borne induced vibrations,

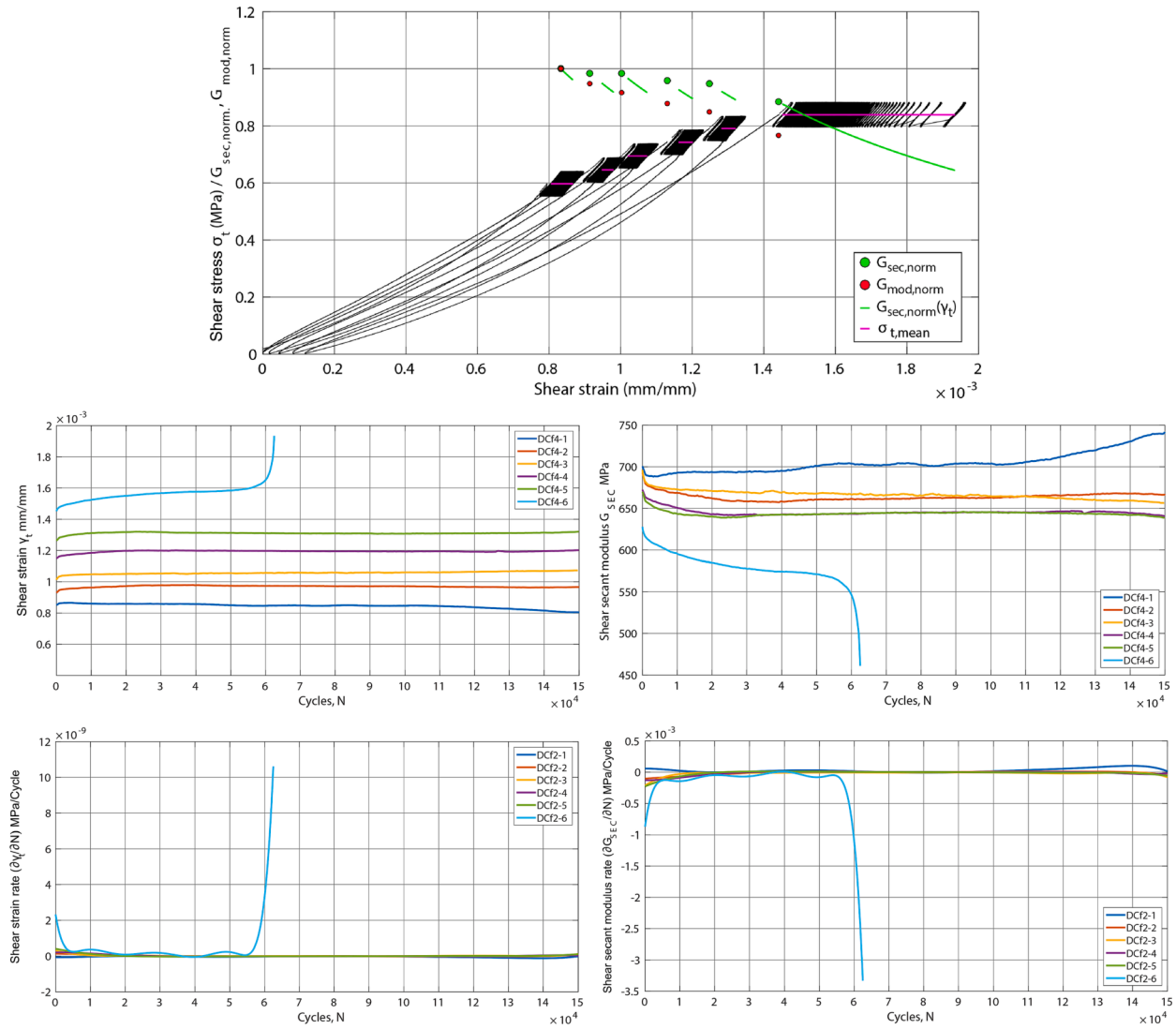

Fig. 13. Fatigue acquisition data, for wallet *DCf4* in diagonal compression: (a) shear stress–strain curve in masonry surface, with the shear elastic and secant modulus, normalized to the initial respective values; average shear strain (b) and secant shear stiffness evolution (c), and their respective rates (d) and (e), with respect to fatigue cycles N.

according to processes explained in Karanikoloudis et al. [41]. Second, boundary conditions and material properties for the evaluated structural elements should be established, namely the local stress state, stiffness evolution, compressive and shear capacity, with the use of minor destructive testing, e.g., single and double compressive and shear flat jack tests, mortar bed joint shear resistance tests etc. Third, a stress–strain investigation should be conducted with nonlinear static numerical analyses in partial numerical models, in order to identify stress concentration areas, in correlation with areas under high induced vibration amplitudes. Fourth, a field fatigue monitoring process should be implemented, with the installation of strain gauges, attached in masonry, covering high shear stress zones and existing crack patterns, which after temperature compensation can verify potential positive trends.

Finally, considering the numerical modelling of fatigue in masonry structures, the commonly used smeared crack models do not account for cyclic deterioration. In fact, 3D material constitutive models with updated yield surfaces are needed, which account for the inelastic cumulative strains and damage under each cycle. Such a 3D orthotropic smeared crack and crack band model is part of the material library in ATENA FE software, which fully incorporates fatigue tensile damage [20]. Here, for the total accounted tensile strain ε_{ij}, decomposed into an elastic ε_{ij}^{e}, plastic ε_{ij}^{p} and fracturing ε_{ij}^{f} strain, an additional fracturing strain increment $\varepsilon_{\text{fatigue}}$ is added after N_i cycles, which is a percentage of the failing strain after N_f cycles. Input material parameters include the knowledge of experimental *S-N*$_f$ curves of masonry, as incorporated in Equation (16), with β_{fatigue}, a material constant, mostly defined within a range of static tensile stresses.

Table 11
Mean and standard deviation of shear strain and secant shear stiffness rates of fatigue Stage II. Note the fatigue branches *DCf3-3* and *DCf4-6* resulting to failure.

		$d(\gamma_{t,Bj,m})/d(N_i)$		$d(G_{sec,Bj,m})/d(N_i)$	
Wallet DCf_{i-j}	Fatigue B_j Stage II	mean	Std	mean	Std
DCf_{2-1}	$N_{30\%}$- $N_{100\%}$	1.30e-11	3.22e-11	−2.48e-05	6.26e-05
DCf_{2-2}	$N_{30\%}$- $N_{100\%}$	1.65e-11	4.66e-11	−2.99e-05	8.55e-05
DCf_{2-3}	$N_{30\%}$- $N_{100\%}$	−3.15e-12	4.31e-11	5.44e-06	7.82e-05
DCf_{2-4}	$N_{30\%}$- $N_{100\%}$	1.35e-11	4.83e-11	−2.42e-05	8.64e-05
DCf_{2-5}	$N_{30\%}$- $N_{100\%}$	1.69e-11	1.69e-11	−2.44e-05	2.49e-05
DCf_{2-6}	$N_{30\%}$- $N_{100\%}$	2.17e-11	4.35e-11	−3.08e-05	6.24e-05
DCf_{2-7}	$N_{30\%}$- $N_{100\%}$	1.85e-11	3.34e-11	−2.28e-05	4.10e-05
DCf_{2-8}	$N_{30\%}$- $N_{100\%}$	2.32e-11	2.14e-11	−2.51e-05	2.35e-05
DCf_{2-9}	$N_{30\%}$- $N_{100\%}$	2.69e-11	3.64e-11	−2.56e-05	3.41e-05
DCf_{2-10}	$N_{30\%}$- $N_{100\%}$	4.54e-11	5.89e-11	−3.96e-05	5.06e-05
DCf_{3-1}	$N_{30\%}$- $N_{100\%}$	1.29E-11	4.15E-11	−1.34E-05	4.30E-05
DCf_{3-2}	$N_{30\%}$- $N_{100\%}$	5.60E-11	6.61E-11	−5.51E-05	6.31E-05
DCf_{3-3}	$N_{10\%}$- $N_{80\%}$	2.76E-10	1.54e-10	−1.68e-04	5.86e-05
DCf_{4-1}	$N_{30\%}$- $N_{100\%}$	−3.87e-11	3.92e-11	3.37e-05	3.46e-05
DCf_{4-2}	$N_{30\%}$- $N_{100\%}$	−7.71e-12	1.40e-11	5.22e-06	9.70e-06
DCf_{4-3}	$N_{30\%}$- $N_{100\%}$	1.57e-11	1.57e-11	−9.96e-06	1.00e-05
DCf_{4-4}	$N_{30\%}$- $N_{100\%}$	2.05e-12	1.85e-11	−1.13e-06	1.03e-05
DCf_{4-5}	$N_{30\%}$- $N_{100\%}$	6.03e-12	2.09e-11	−3.17e-06	1.10e-05
DCf_{4-6}	$N_{10\%}$- $N_{80\%}$	1.52e-10	1.13e-10	−6.09e-05	4.24e-05

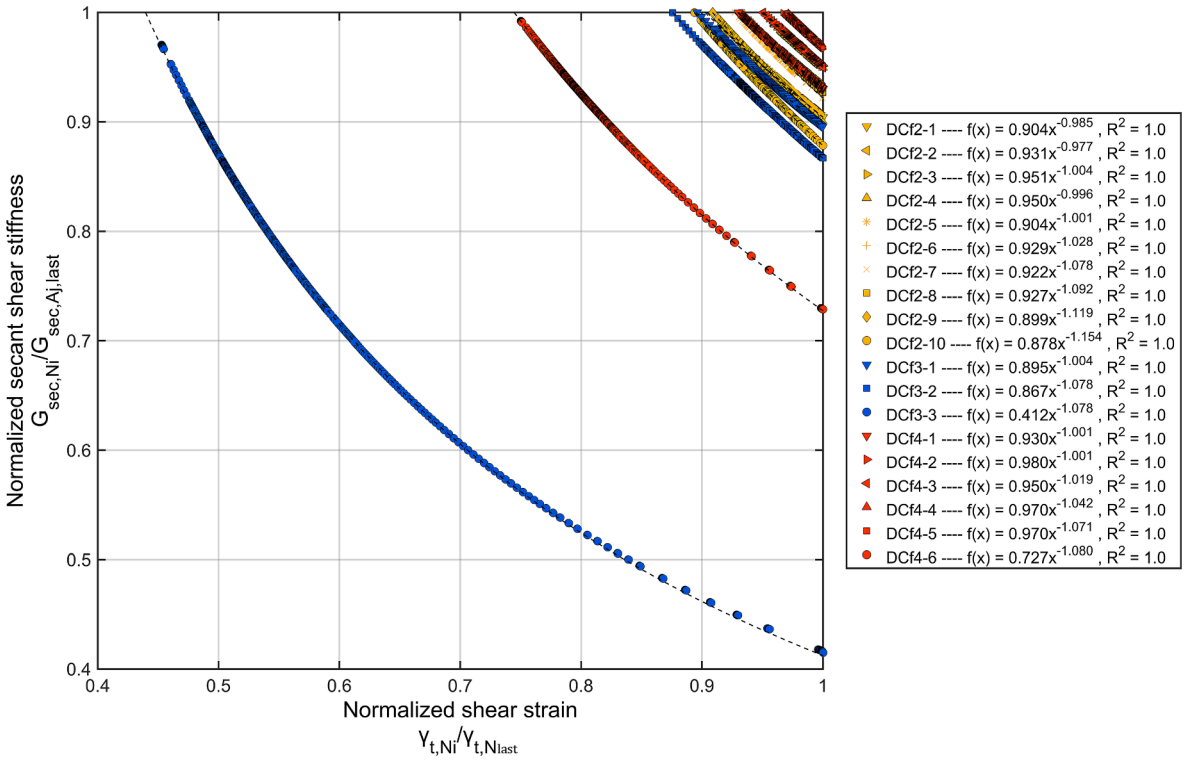

Fig. 14. Exponential decay curve fitting of the normalized secant shear stiffness versus the normalized shear strain, of the various fatigue tests of *DCf2-j*, *DCf3-j* and *DCf4-j*. Note the two complete fatigue tests *DCf3-3* and *DCf4-6* leading to failure.

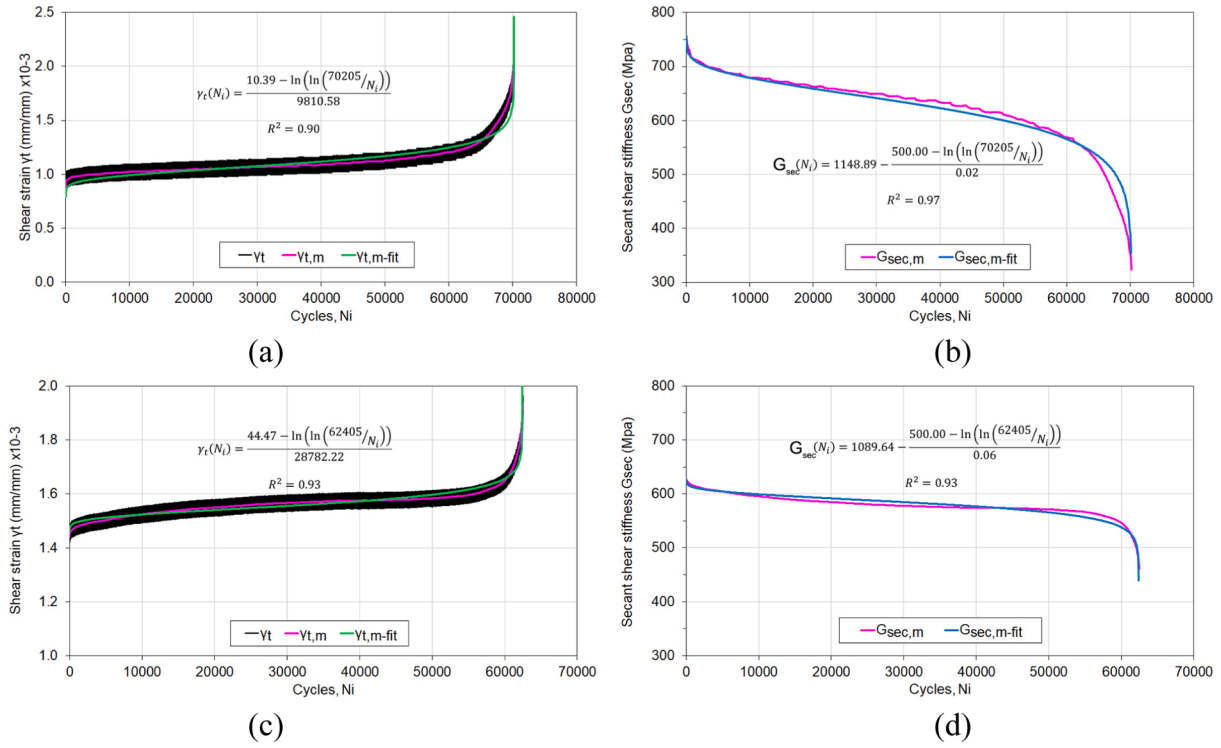

Fig. 15. Fatigue data fits with a reverse Gompertz curve for the average shear strain and secant shear stiffness for $DCf_{3\text{-}3}$ (a) and (b) and $DCf_{4\text{-}6}$ (c) and (d) respectively.

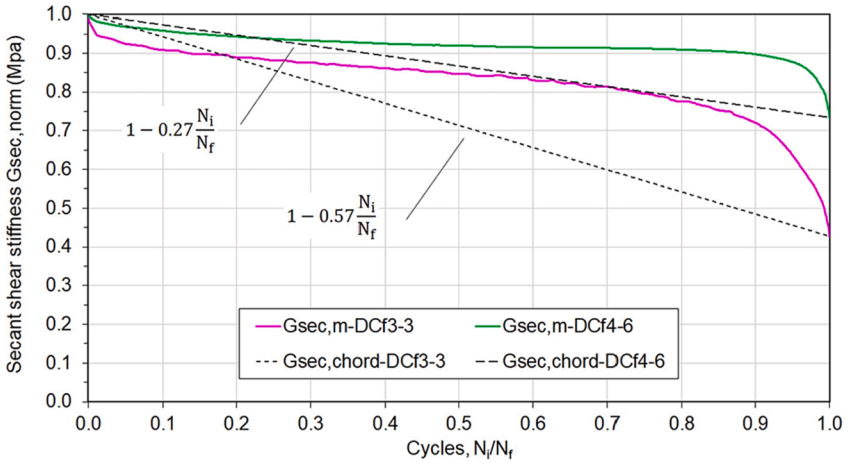

Fig. 16. End to end linear piecewise function for normalized secant shear stiffness evolution and normalized cycles, for fatigue branches $DCf_{3\text{-}3}$ and $DCf_{4\text{-}6}$.

$$\frac{\sigma_{max}}{f_t} = 1 - \beta_{fatigue}(1 - R)logN_f \tag{16}$$

Conclusions

In general, fatigue long-term effects in historic masonry structures, have not been fully evaluated and many times are not incorporated in the structural assessment framework. Of particular use are the formation of fatigue stress and strain curves (S-N_f and ε-N_f), according to the number of cycles until failure N_f. In fact, fatigue strain softening in masonry is a catalytic factor for the stress–strain relationship, and by extension to the decay of the elastic and secant stiffness, up to ultimate failure. Of particular interest is fatigue loading in masonry under diagonal compression actions, considering the low levels of tensile strength f_t. In particular, at locations of

Table 12
Estimated fatigue cycles to failure for incomplete fatigue branches, according to the obtained end to end linear piecewise functions, for each of the tested wallets $DCf_{3\text{-}(1\text{-}2)}$ and $DCf_{4\text{-}(1\text{-}5)}$. Note the deterministic fatigue cycles until failure for fatigue branches $DCf_{3\text{-}3}$ and $DCf_{4\text{-}6}$.

Wallet DCfi-j	Fatigue Bj Cycles	$G_{sec,N=1}$	$G_{sec,N_{Bj}}$	λ	$N_{f,est} = \frac{\lambda N_{Bj}}{1-\frac{G_{sec}, N_{Bj}}{G_{sec}, N=1}}$
DCf3-1(0.63f_t,±0.12f_t)	1–1.5E + 05	830.4	743.5	0.57	8.21E + 05
DCf3-2(0.69f_t,±0.12f_t)	1–1.5E + 05	837.6	726.2		6.46E + 05
DCf3-3(0.75f_t,±0.12f_t)	7.02E + 04	756.5	323.4		7.02E + 04
DCf4-1(0.64ft,±0.04ft)	1–1.5E + 05	691.1	740.3	0.27	–
DCf4-2(0.69ft,±0.04ft)	1–1.5E + 05	680.0	666.5		2.01E + 06
DCf4-3(0.73ft,±0.04ft)	1–1.5E + 05	692.0	657.3		7.94E + 05
DCf4-4(0.79ft,±0.04ft)	1–1.5E + 05	663.6	641.5		1.20E + 06
DCf4-5(0.84ft,±0.04ft)	1–1.5E + 05	659.3	638.2		1.24E + 06
DCf4-6(0.89ft,±0.04ft)	6.25E + 04	628.0	461.1		6.25E + 04

tensile stress concentration, i.e., $\geq 0.70f_t$, where the transition to macrocracking is already established, or is even closer to failure, i.e., $\geq 0.90f_t$), where crack growth is considered highly unstable, fatigue loading at medium to low levels can lead to stiffness degradation and failure. Thus, the knowledge of residual material properties for masonry and their rate of deterioration over time, is of interest.

Experimental, fatigue loading protocols, are configured as continuous cyclic quasi-static sinusoidal loading, under force control, with the conversion from ground-borne vibrations to equivalent displacement or force amplitudes, formed through stiffness functions. First and foremost, static and fatigue stress combinations in masonry, to be replicated experimentally, should be defined under in-situ observations. Hence, instead of assessing fatigue under constant shear stress levels, one should also account for progressively increasing ones, in case of time-varying loading conditions, e.g., a dead load increase from structural interventions and a change of load paths from settlements, earthquakes or accidental actions. Here, each fatigue loading combination can be considered as an independent fatigue test, defined by the end-to-end shear secant stiffness and shear strain values.

For the assessment of fatigue loading and corresponding fatigue life in masonry specimens, the knowledge of static mechanical properties and stress–strain curves is essential, with average values obtained under a sufficient number of specimens. As demonstrated from several tested brick masonry wallets, with and without render, the normalized, average, ascended part of the quasi-static diagonal compression stress–strain curve, represents an optimal response, formed under high correlation. Thus, together with the knowledge of the elastic stiffness of the wallet of interest, obtained under a quasi-static preload, a sufficient estimation of the peak shear strength and strain, and the envelop fit curve can be obtained.

The current work focused on experimental fatigue tests under diagonal compression in three simulated historic solid brick and lime mortar masonry wallets, with one-sided, lime-based rendering. Under combinations of a constant shear stress rate $\Delta\sigma$, set at a medium to low level, and a high static shear loading σ_m, increasing progressively, fatigue tests considered a certain number of cycles, representative of 1.5 years of passing trains, with the main objective set on quantifying levels of damage, stiffness degradation and failure. In conclusion, corresponding groundborne vibrations with peak particle velocities higher than 8 mm/s, for a 50–100 Hz dominant frequency range, under a high static diagonal compression in the range of 0.6–0.9f_t, resulted to cracking and local shear failure at relatively low number of cycles, around 10^5-10^6 or 7–9 months, accounting for the frequency of passing trains. Even if fatigue tensile cracking will not result to global structural failures or instabilities, local discontinuities are bound to arise, and pre-existing cracks may evolve, with focus on areas of stress concentrations, e.g., windowsills, arches, shear connectors, walls under in-plane actions etc. Considering the secant shear stiffness evolution during constant fatigue loading, even under a gradual increase in static loading, it follows a somewhat steady decrease, besides the last, tertiary Stage III, which is considered to increase exponentially. In addition, normalized secant shear stiffness and shear strain average amplitudes, under fatigue loading combinations of maximum shear stress amplitudes σ_{max} higher than 0.7f_t, followed an exponential, reverse power law, with higher strain relaxation rates.

In addition, from the experimental fatigue tests resulting to failure, the constructed fatigue curves for the average shear strain (γ_f-N_f), and the shear secant stiffness (G_{sec}-N_f), were fitted with a reversed non-symmetrical sigmoid function of the Gompertz equation, under a high achieved correlation. In fact, shear stiffness and tensile strength degradation, during various fatigue load combinations, under the hypothesis of equal fatigue properties, can be associated directly, when normalized with initial values, prior to fatigue. Thus, under end-to-end linear piecewise functions of normalized fatigue properties and normalized fatigue cycles, fatigue life estimates can be attempted, where failure has not yet been reached.

In conclusion, the need for determining experimentally probabilistic distribution functions for fatigue in masonry, for different masonry typologies, material constituents, and a full range of static and cyclic stress combinations, is essential to incorporate fatigue damage into multi-hazard assessment processes for cultural heritage buildings.

Declaration of Competing Interest

The authors declare that they have no known competing financial interests or personal relationships that could have appeared to influence the work reported in this paper.

Data availability

Data will be made available on request.

Acknowledgements

The current work was partly supported by FCT (Portuguese Foundation for Science and Technology), within the INFRARISK PhD program and ISISE, project UID/ECI/04029/2013.

References

[1] D. Abrams, J. Noland, R. Atkinson, P. Waugh, Response of Clay-Unit Masonry to Repeated Compressive Forces, 1985.
[2] J.M. Adell Argilés, 19th century brick architecture: rationality and modernity, Inf. Constr. 44 (421) (1992) 5–15, https://doi.org/10.3989/ic.1992.v44.i421.1309, in Spanish.
[3] ASTM C469/C469M-14, Standard Test Method for Static Modulus of Elasticity and Poisson's Ratio of Concrete in Compression, ASTM International, West Conshohocken, PA, 2014 www.astm.org.
[4] ASTM C67/C67M-20, Standard Test Methods for Sampling and Testing Brick and Structural Clay Tile, ASTM International, West Conshohocken, PA, 2020 www.astm.org.
[5] ASTM E519/E519M-20, Standard Test Method for Diagonal Tension (Shear) in Masonry Assemblages, ASTM International, West Conshohocken, PA, 2020 www.astm.org.
[6] BD 91/04-14, Design Manual for Roads and Bridges, Volume 2 Highway Structures: Design (Substructures and Special Structures) Materials, Section 2 Special Structures, Part 14, Unreinforced Masonry Arch Bridges, Stationery Office, London, 2004.
[7] L. Binda (Ed.), Learning from Failure, Long-term Behavior of Heavy Masonry Structures, WIT Press, Southampton, 2008.
[8] J.J. Brooks, Concrete and Masonry Movements, Chapter 5 - Elasticity of Masonry, Butterworth-Heinemann, 2015, pp. 95–136, doi: 10.1016/B978-0-12-801525-4.00005-4.
[9] BS 5228-2:2009, Code of Practice for Noise and Vibration Control on Construction and Open Sites – Part 2: Vibration, British Standard, 2009.
[10] BS 7385-2:1993, Evaluation and Measurement for Vibration in Buildings – Part 2: Guide to Damage Levels from Groundborne Vibration, British Standard, 1993.
[11] BS EN 10080, Steel for the Reinforcement of Concrete - Weldable Reinforcing Steel – General, BSI British Standards, 2005.
[12] BS EN 1015-2:1998, Methods of Test for Mortar for Masonry-Part 2: Bulk Sampling of Mortars and Preparation of Test Mortars, CEN, Brussels, 1998.
[13] BS EN 1052-1:1999, Methods of Test for Masonry - Part 1: Determination of Compressive Strength, CEN, Brussels, 1999.
[14] BS EN 772-1:2011, Methods of Test for Masonry Units. Determination of Compressive Strength +A1:2015, CEN, Brussels, 2011.
[15] BS EN 998-2:2003, Specification for Mortar for Masonry - Part 2: Masonry Mortar, CEN, Brussels, 2003.
[16] A. Carpinteri, A. Grazzini, G. Lacidogna, A. Manuello, Durability evaluation of reinforced masonry by fatigue tests and acoustic emission technique, Struct. Control Health Monit. 21 (2014) 950–961, https://doi.org/10.1002/stc.1623.
[17] A. Carpinteri, M. Paggi, A unified interpretation of the power laws in fatigue and the analytical correlations between cyclic properties of engineering materials, Int. J. Fatigue 31 (2009) 1524–1531, https://doi.org/10.1016/j.ijfatigue.2009.04.014.
[18] J.R. Casas, A probabilistic fatigue strength model for brick masonry under compression, Constr. Build. Mater. 23 (8) (2009) 2964–2972, https://doi.org/10.1016/j.conbuildmat.2009.02.043.
[19] J.R. Casas, Reliability-based assessment of masonry arch bridges, Constr. Build. Mater. 25 (2011) (2010) 1621–1631.
[20] V. Červenka, L. Jendele, J. Červenka, ATENA Program Documentation Part 1, Theory, Červenka Consulting s.r.o., 2021.
[21] P. Chabat, La Brique et la Terre Cuite. Étude historique; fabraication et usages, Paris (in French), 1886.
[22] M. Como, Springer Series in Solid and Structural Mechanics, Volume 5, Springer International Publishing AG, Switzerland, 2016, doi 10.1007/978-3-319-24569-0.
[23] Concrete Material Use Strain Gauge, Concrete Material Use Strain Gauge, Tokyo Measuring Instruments Laboratory Co., Ltd. (n.d.), 2021. Available from: <https://tml.jp/e/product/strain_gauge/concrete.html>.
[24] M. Corradi, R. Sisti, A. Borri, Effect of thin cement-based renders on the structural response of masonry wall panels, Appl. Sci. 8 (2018) 98, https://doi.org/10.3390/app8010098.
[25] DIN 4150-3:2016, Structural Vibration in Buildings – Effects on Structures, Deutsches Institut für Normung, 2016.
[26] N.E. Dowling, Mechanical Behavior of Materials: Engineering Methods for Deformation, Fracture, and Fatigue, Pearson Prentice Hall, Upper Saddle River, NJ, USA, 2007.
[27] E.N. Dvorkin, A.M. Cuitiño, G. Gioia, A concrete material model based on non-associated plasticity and fracture, Eng. Comput. 6 (4) (1989) 281–294, doi: 10.1108/eb023783.
[28] EN 1992-1-1, Design of Concrete Structures - Part 1–1: General Rules and Rules for Buildings, CEN, Brussels, 2004.
[29] EN 998–1, Specification for Mortar for Masonry - Part 1: Rendering and Plastering Mortar, CEN, Brussels, 2016.
[30] EN 1996-1-1, Design of Masonry Structures - Part 1–1: General Rules for Reinforced and Unreinforced Masonry Structures, CEN, Brussels, 2005.
[31] L. Facconi, F. Minelli, J.F. Vecchio, Predicting uniaxial cyclic compressive behavior of brick masonry: new analytical model, J. Struct. Eng. 144 (2) (2018) 04017213, https://doi.org/10.1061/(ASCE)ST.1943-541X.0001961.
[32] FIB Model Code, FIB Model Code for Concrete Structures 2010, International Federation for Structural Concrete, Lausanne, Switzerland, 2013.
[33] G.A. Gazonas, M.J. Scheidler, A.P. Velo, Exact analytical solutions for elastodynamic impact, Int. J. Solids Struct. 75–76 (2015) 172–187, doi: 10.1016/j.ijsolstr.2015.08.011.
[34] GB/T 50452, Technical Specifications for Protection of Historic Buildings Against Man-made Vibration, National Standard of the People's Republic of China, 2008.
[35] G. Glinka, Calculation of inelastic notch-tip strain-stress histories under cyclic loading, Eng. Fract. Mech. 22 (5) (1985) 839–854.
[36] J.O. Holmen, Fatigue of concrete by constant and variable amplitude loading, Fatigue of Concrete Structures, ACI Special Publication 75, American Concrete Institute, Detroit, 1982, pp. 71–110.
[37] J. Hoshikuma, K. Kawashima, K. Nagaya, A.W. Taylor, Stress-strain model for confined reinforced concrete in bridge piers, J. Eng. Struct. 123:5(624) 624–633, doi: 10.1061/(ASCE)0733-9445(1997).
[38] Y. Hu, J. Shi, X. Cao, J. Zhi, Low cycle fatigue life assessment based on the accumulated plastic strain energy density, Materials 14 (2021) 2372, https://doi.org/10.3390/ma14092372.
[39] ISO 4866:1990, Mechanical Vibration and Shock – Vibration of Buildings – Guidelines for the Measurement of Vibrations and Evaluation of Their Effects on Buildings, International Organization for Standardization, 1990.
[40] D. Jukic, G. Kralikb, R. Scitovskia, Least-squares fitting Gompertz curve, J. Comput. Appl. Math. 169 (2004) 359–375, https://doi.org/10.1016/j.cam.2003.12.030.
[41] G. Karanikoloudis, P.B. Lourenço, N. Mendes, B. Serra, R. Boroschek, Monitoring of induced groundborne vibrations in cultural heritage buildings. Miscellaneous errors and aliasing through integration and filtering, Int. J. Arch. Heritage (2021), https://doi.org/10.1080/15583058.2020.1802532.

[42] I.S. Koltsida, A.K. Tomor, C.A. Booth, Experimental evaluation of changes in strain under compressive fatigue loading of brick masonry, Constr. Build. Mater. 162 (2018) 104–112, doi: 10.1016/j.conbuildmat.2017.12.016.
[43] I.S. Koltsida, A.K. Tomor, C.A. Booth, Probability of fatigue failure in brick masonry under compressive loading, Int. J. Fatigue 112 (2018) 233–239, doi: 10.1016/j.ijfatigue.2018.03.023.
[44] J. Lacroux, C. Détain, Constructions en briques. La brique ordinaire au point de vue décoratif, de la société Centrale des Architectes des oeuvres de M. César Daly, Paris (in French), 1878.
[45] P.B. Lourenco, Computational Strategies for Masonry Structures, PhD Thesis, Delft University of Technology, Civil Engineering Department, Delft University Press, Netherlands, 1996.
[46] C. Melbourne, A.K. Tomor, J. Wang, Cyclic load capacity and endurance limit of multi-ring masonry arches, Arch Bridges, ARCḤ04 2004 Barcelona.
[47] NA to BS EN 1996-1-1:2005, UK National Annex to Eurocode 6: Design of Masonry Structures - Part 1-1: General Rules for Reinforced and Unreinforced Masonry Structures, BSI, 2007.
[48] NHL 5, Cal hidráulica natural NHL 5, Ficha técnica, Declaração de desempenho, Ficha de dados de segurança, Secil, Lisbon (in portuguese), 2014. Available from: <https://secilpro.com/produtos/tipos_aplicacao/reabilitacao-e-restauro/alvenarias-antigas/cal-hidraulica-natural-nhl-5>.
[49] T. Nicholas, High Cycle Fatigue: A Mechanics of Materials Perspective, first ed., Elsevier Ltd., Oxford, UK, 2006.
[50] NTC, Norme tecniche per le costruzioni. With Circolare from January 21, no. 7 (2019) from Ministry of infrastructure and transportation. Italy (in Italian), 2018.
[51] REABILITA CAL CS, Argamassa de consolidação de alvenarias antigas exclusivamente formulada com cal hidráulica natural, Ficha técnica, Declaração de desempenho, Ficha de dados de segurança, Secil, Lisbon (in portuguese), 2019. Available from: https://www.seciltek.com/documentos/reabilita.
[52] T. Roberts, T. Hughes, V. Dandamudi, B. Bell, Quasi-static and high cycle fatigue strength of brick masonry, Constr. Build. Mater. 20 (9) (2006) 603–614.
[53] P. Ronca, A. Franchi, P. Crespi, Structural failure of historic buildings: masonry fatigue tests for an interpretation model, in: Lourenço, Roca (Eds.), Structural Analysis of Historical Constructions - 2 Volume Set - Modena, 2005, doi: 10.1201/9781482288377.
[54] SN 604312A, Effects of Vibration on Construction, Swiss Standards Association, 1992.
[55] M. Tomazevic, Earthquake-resistance design of masonry buildings, Imperial College Press, London, UK, 1999.